Numerical Investigation of $C_{L,\text{max}}$ Prediction on the NASA High-Lift Common Research Model [*]

Oliver M. F. Browne[†], Jeffrey A. Housman[‡], Gaetan K. Kenway[§], Aditya S. Ghate[¶] and Cetin C. Kiris[‖]

NASA Ames Research Center, Moffett Field, CA 94035

An assessment of a Hybrid RANS/LES (HRLES) approach for $C_{L,\text{max}}$ prediction is presented for the NASA High-Lift Common Research Model (CRM-HL). Both free air and wind tunnel configurations of the CRM-HL are investigated and the results are compared to the QinetiQ wind tunnel experiments and two other numerical approaches: Reynolds Averaged Navier-Stokes (RANS) and Wall-Modeled Large Eddy Simulations (WMLES). For the free-air configuration, HRLES is shown to address some of the known shortcomings with RANS and prevent inboard and outboard flow separation particularly in the region of $C_{L,\text{max}}$ and post-stall. To achieve these improvements over RANS, LES-appropriate grids and numerical discretizations are required. It was also found that when applying HRLES to a RANS best practice grid and numerics that the HRLES method significantly underperformed RANS. For the in-tunnel configuration, HRLES showed good agreement with the loads, surface pressure and oil-flow photographs obtained in the experiment. HRLES was able to improve upon the RANS simulations, which showed a sharp loss of lift at the two highest angles-of-attack due to large scale inboard and outboard separation on the wing, by correctly predicting the corner flow separation and showing remarkably close agreement in the flow topologies with the experiment.

Nomenclature

c_f	=	skin friction coefficient
C_D	=	drag coefficient
C_L	=	lift coefficient
$C_{L,\text{max}}$	=	maximum lift coefficient
c_{MAC}	=	mean aerodynamic chord
C_{My}	=	pitching moment coefficient

C_p	=	pressure coefficient
f_d	=	shielding function
CTU	=	convective time unit
M	=	Mach number
Re	=	Reynolds number
y^+	=	dimensionless wall distance
α	=	angle of attack, deg
δ_{bl}	=	Boundary layer height
Δt	=	timestep size
η	=	dimensionless spanwise distance from centerline
$\tilde{\nu}$	=	Spalart-Allmaras transported pseudo eddy-viscosity

I. Introduction

Accurate computational predictions of the aerodynamics seen on conventional aircraft with swept medium to high aspect ratio wings in high-lift configurations (take-off/landing) are notoriously challenging[1]. The flowfield seen in such configurations is dominated by the strong interplay between turbulent boundary layer flow separation, a variety of off-body vortex tubes and complex wakes merging into boundary layers in the presence of high pressure gradients[2]. This problem has been the focus of three past AIAA High Lift Prediction Workshops (HLPW), and the large scatter seen in submissions[3] underscores the need for a systematic evaluation of the current state-of-the-art Computational Fluid Dynamics (CFD) tools to understand potential benefits that are offered by different methodologies. This is particularly important to enable analysis-based compliance for aircraft certification as envisaged in numerous programmatic objectives over the next two decades[4–6].

The previous HLPW workshops largely focused on Reynolds-averaged Navier-Stokes (RANS) methods and it was shown across all workshops that RANS is an unreliable tool in the region of $C_{L,\max}$[7]. This unreliability has motivated the move to scale-resolving simulations such as Wall-Modeled Large Eddy Simulations (WMLES) and Hybrid RANS/LES (HRLES), with the focus of the current paper being on the latter. Under the overarching goal of *Certification by Analysis* (CbA)[8], the present work aims to provide insight to the following questions in the context of high-lift aerodynamics:

1) **Is HRLES a computationally feasible solution to overcome and address the failures seen in RANS?** The CFD results for the JAXA Standard Model presented at the previous High Lift Prediction Workshop, namely HLPW3[3], which was conducted in 2017, showed significant improvement in the aerodynamic load predictions in the low and mid angle-of-attack (AoA) range when compared with the previous workshops. However, no

material improvement was seen in the high AoA range in the region of $C_{L,\max}$. Furthermore, the RANS based models appeared to incorrectly (qualitatively) predict the flow near the wing-tips, which was visualized as an over-prediction of the separated flow extent near the wing tips. It is outlined in the summary paper (see Ref. [7]) of the current iteration, HLPW4[9], that RANS is still an unreliable tool for predicting the forces/moment accurately and consistently for high-lift aircraft geometries. The present work will look to establish whether or not HRLES can address the shortcomings of RANS in a computationally viable manner.

2) **What are the best practices for HRLES scale resolving simulations for $C_{L,\mathbf{max}}$ prediction?** Since hybrid RANS/LES methods are both philosophically and practically interpreted as incremental modifications to RANS closures, we wish to appraise the performance of HRLES in the context of equivalent RANS simulations. Towards this, we first delineate the fundamental grid requirements for the method, and hope to address the question of whether RANS-best practices for grid (and numerical discretization) can be inherited by HRLES (as is the common practice in the application engineering community). While prior work on $C_{L,\max}$ prediction using both isotropic, immersed boundary[10] as well as unstructured body-fitted[11] formulations have shown promise, the present work is focused on establishing best practices for HRLES that would enable its use in a predictive setting. A previous HRLES study by the authors, for the NASA Juncture Flow Model, showed a strong sensitivity to mesh resolution, namely; when moving to higher mesh resolutions, inferior predictions in the separated flow region were obtained[12]. This earlier work used an older version of the shielding function employed in this study (see Sec. II.A).

3) **What are the sensitivities of HRLES solution to aspects such as underlying RANS closure and initial condition *etc*?** Large sensitivities were found in the integrated aerodynamic loads and flow topology by the authors [13] for steady-state RANS results with various SA closures for the CRM-HL. In fact, relatively large sensitivities were also seen for simulations which employed the same SA closure and same grid (although different connectivity procedure) with different CFD solvers for steady-state RANS simulations on CRM-HL [14] - these issues may be partially or fully explained by differing degrees of residual convergence. RANS is relatively cheap when compared to scale resolving simulations and more easily affordable to run cases with different SA closure models. However, if HRLES is to become an effective and reliable tool in $C_{L,\max}$ and post-stall prediction, the sensitivity of the solution to the underlying closure model needs be understood. We also need to determine whether the closure model is a leading order on the predicted solution. RANS approaches have been shown to have multiple solution branches depending on how the flow is initialized, *i.e. "cold-start", "warm-start", "pitch-and-pause", etc*), (see Ref. [15] for RANS results comparing *"cold-start"* to *"warm-start"* for JAXA Standard Model from HLPW3). As such, the sensitivity of HRLES to flow initial conditions should also be investigated.

The geometry considered in this work is the NASA semispan High Lift Common Research Model (CRM-HL) which
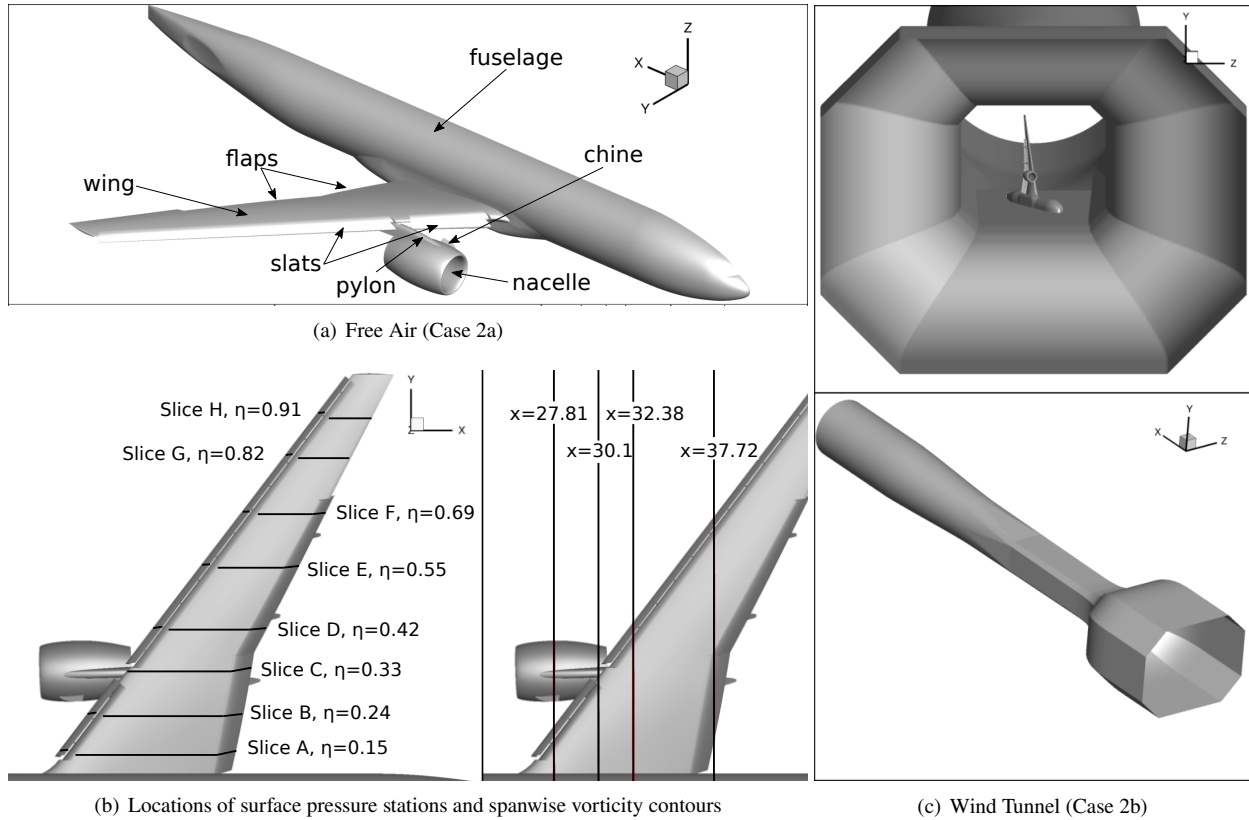
(a) Free Air (Case 2a)

Slice H, η=0.91
Slice G, η=0.82
Slice F, η=0.69
Slice E, η=0.55
Slice D, η=0.42
Slice C, η=0.33
Slice B, η=0.24
Slice A, η=0.15

x=27.81 x=32.38
x=30.1 x=37.72

(b) Locations of surface pressure stations and spanwise vorticity contours

(c) Wind Tunnel (Case 2b)

Fig. 1   A schematic of the NASA semispan High Lift Common Research Model (CRM-HL) test article that was studied (free air and wind tunnnel configurations) and the locations where particular flow quantities were recorded and used for comparison and validation.

is a representative geometry of a modern commercial airliner[16]. The benchmark experiment used to compare the HRLES results is that of Evans *et al.* (2020)[17] studying the NASA 10% half-span model (see Fig. 1) in the QinetiQ 5-meter wind tunnel (5mWT) located in Farnborough, UK. This configuration is also being evaluated as part of Case 2 in the 4th AIAA High-Lift Prediction Workshop (2022)[9]. Beyond the geometry definitions provided, the entire problem is characterized by a mean-aerodynamic chord based Reynolds number of 5.5×10^6 and a free-stream (and test section) Mach number of 0.2. Case 2 consisted of sub cases Case 2a and 2b which were the free air and wind tunnel configurations, respectively. Case 2a simulations are compared with a set of corrected loads and moments. The corrected and uncorrected aerodynamic loads, oil flow images, pressure coefficients at various spanwise stations, as well as details about the CRM-HL geometry are open-source and distributed via the HLPW4 webpage[9].

All computational evaluations use the structured curvilinear overset compressible Navier-Stokes formulation within the Launch, Ascent, and Vehicle Aerodynamics (LAVA) computational framework[18]. This paper is a continuation of the work that was presented in the summary paper by Kiris *et al.*[13] which compared RANS, HRLES and WMLES results, using the LAVA solver, for HLPW4. A previous version of this paper was first presented at the AIAA Aviation 2022 Forum in Chicago, IL (see Ref. [19]).

The rest of the paper is outlined as follows - we begin with a discussion of the shielding function and turbulence closure in Sec. II and Sec. II.B describes the general numerical discretization. Then we introduce the different grid systems in Sec. III. The results section, Sec. IV, is split into two parts: Sec. IV.A presents the results for the free-air configuration and Sec. IV.B presents the results for the in-tunnel configuration simulations. Finally, the concluding remarks are provided in Sec. V.

II. Turbulence Model and Numerical Discretization

A. HRLES Shielding Function and Underlying RANS Closure

The hybrid RANS/LES (HRLES) approach employed in this work is the Zonal Detached Eddy Simulation (ZDES) 2020 mode 2 Enhanced Protection (EP) [20] method. The ZDES2020 mode 2 EP method builds upon and attempts to alleviate the shortcomings of previous iterations of automatic shielding functions developed (*e.g.* Delayed Detached Eddy Simulations, DDES2006 [21] and ZDES2012 mode 2 [22]), with an improved shielding function f_d that should better protect the boundary-layer by staying in RANS mode ($f_d = 0$) for attached flows even in the limit of small Δ/δ_{bl}. Earlier DDES approaches are prone to prematurely going into LES mode ($f_d = 1$) despite the lack of LES (scale resolving) grid spacings. This sudden loss of modeled-stress which is not compensated for by any resolved content (resolved Reynolds stress) leads to the well known phenomenon called modeled stress depletion. The ZDES2020 mode 2 EP has previously been validated and used in LAVA[23] and the reader is referred to prior publications[24, 25] for further implementation-specific details. The maximum edge length for a grid-cell serves as the local length scale used in the LES SGS closure.

The Reynolds averaged Navier-Stokes equations are developed using Favre averaging which results in a Reynolds stress tensor which must be modeled to close the governing system of equations. For this paper, the Spalart-Allmaras (SA)[26] turbulence model is the primary turbulence closure being investigated. The SA-neg[27] variant of the model, which modifies the SA equation for $\tilde{\nu} < 0$, is the formulation employed but it is referred to as solely SA, for brevity, for the rest of the paper. Three corrections to the model are also investigated: a) The Rotation Curvature correction[28] which tries to account for streamline curvature in the turbulence production, b) Quadratic Constitutive Relation (QCR2000) correction [29] which replaces the Boussinesq linear eddy viscosity hypothesis with a nonlinear relation, and c) a low-Reynolds number correction [30] which attempts to improve the early development of the boundary layer when the effective Reynolds number is low. While newer versions[31] of the QCR correction have been implemented in LAVA, the versions proposed in Spalart et al. (2000)[29] was used in this work due to its superior convergence properties. Note that the current implementation of RC closure in the LAVA solver does not include the time derivative term which is a term that is part of the Lagrangian (material) derivative of the strain rate tensor.

B. Numerical Discretization

High-order accurate low dissipation finite-difference schemes have been shown to be an accurate and efficient strategy for turbulence resolving simulations using LAVA[24, 25, 32, 33]. A thorough study comparing several high-order finite difference methods on Cartesian grids within the LAVA framework was reported previously[34]. Results from this study indicated that high-order Weighted Essentially Non-Oscillatory (WENO) schemes[35] performed well in both resolution (Points-Per-Wavelength PPW), shock capturing, and robustness under harsh flow conditions. A natural extension of finite-difference WENO schemes to curvilinear grids are the high-order Weighted Compact Nonlinear Schemes (WCNS)[36]. The third-order WCNS was deemed too dissipative for scale resolving simulations during the initial set of simulations performed. Therefore a blended third order upwind/fourth-order centered accurate scheme with a modified Roe scheme (Riemann solver) was utilized for the convective terms. For time integration, a BDF2 discretization is used in physical time, along with pseudo-time embedding and ILU(1) preconditioned GMRES (see Ref. [13] for more details).

III. Curvilinear Overset Grid System

Table 1   Description of the RANS and HRLES grids.

Name	Solve Points	Target y^+	Max Stretching Ratio	Comments
Grid R-C	224M	1.0	1.10	[37]
Grid R-D	550M	0.75	1.07	[37]
Grid H-A	365M	1.0	1.10	inboard + outboard refinement
Grid H-B	325M	1.0	1.10	modified slat wake grid + outboard refinement
Grid H-C	421M	1.0	1.10	outboard refinement
Grid H-D	571M	1.0	1.10	inboard + midboard + nacelle refinement

The updates to purpose-built RANS grids (with $\Delta y^+ \leq O(1)$) to enable HRLES are outlined. The initial approach for HRLES was to utilize the RANS grids, namely Grid R-B and R-C, described in Ref. [13]. This was to establish whether any direct improvement, over RANS, is obtained by simply *"switching on"* the HRLES solver. Subsequently, the RANS grid (Grid R-C) was modified and refined to be more appropriate for a scale resolving simulation. The grid refinement process was conducted in a systematic way but for brevity, only the direct differences between Grid R-C and the final HRLES mesh, H-D, will be described (see Table 1). The main improvements and modifications were:
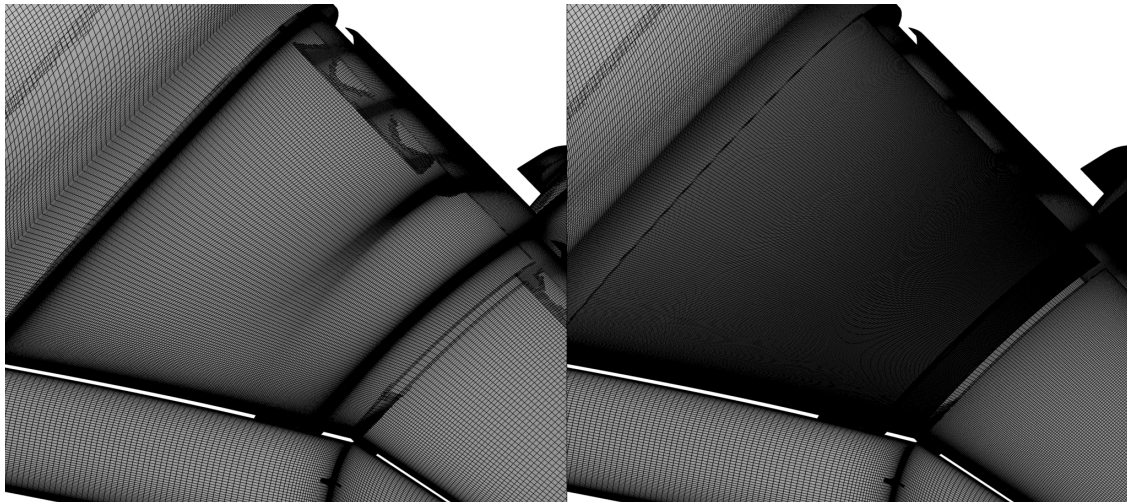
- The initial HRLES simulations on the RANS grids showed significant outboard separation (*e.g* see Fig. 5.g and 5.l), at $C_{L,\max}$ and post-stall angles, that was clearly not present in the experimental results. This was also seen in
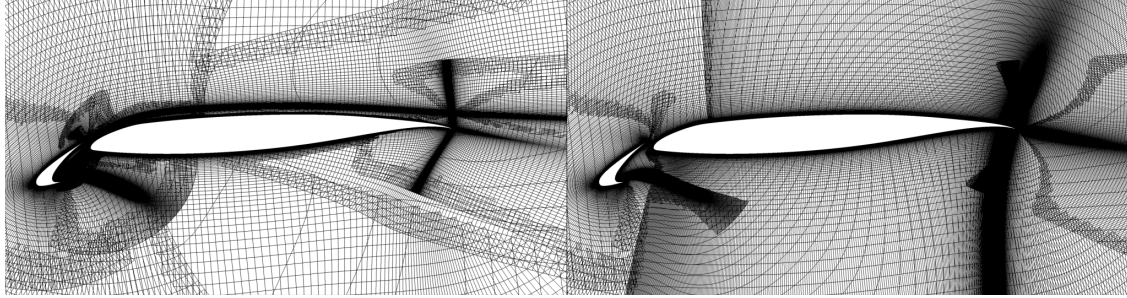
(a) Outboard wing (*y* = 24 m.)
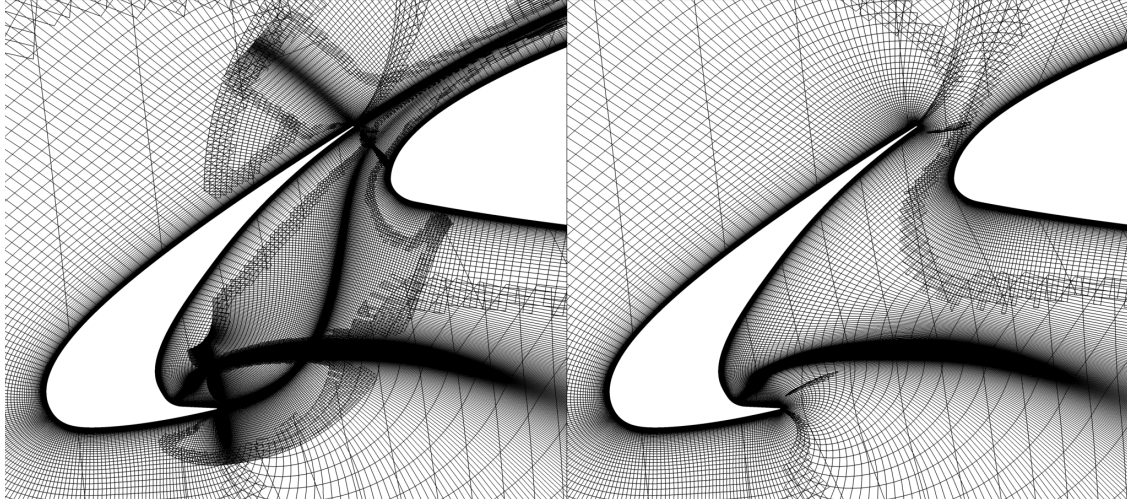
(b) Slat element (*y* = 15 m.)

(c) Inboard wing upper surface

Fig. 2 Volume grid comparisons for the RANS (left) and HRLES (right) meshes.

the RANS results - some dependence on SA closure model and grid resolution - although for baseline SA the separation became more significant with increasing grid resolution. On the RANS Grid R-C, the DDES model was not able to delay or prevent this outboard separation. Therefore, the outboard region of the wing was significantly

refined for HLRES Grid H-D - 8× streamwise and 16× spanwise when compared to Grid R-C (see Fig. 2a).

- HRLES simulations on Grid R-C also showed that in the slat wake the shielding function (f_d) remained in RANS mode for a protracted extent downstream of the slat due to the high-aspect ratio cells which prevented the model from switching to LES mode. Particularly in the outboard section of the wing, when comparing with WMLES solution, the slat wake seemed to be energizing the boundary-layer on the main element and potentially helping it remain attached for longer. To alleviate this issue and allow for the slat wake to transition into LES mode sooner, the grid clustering was modified and the grid points were redistributed to ensure lower aspect ratio cells were in the slat wake which are more appropriate for resolving the fluctuations in the slat wake (see Fig. 2b). This issue is also addressed in Sec. IV.A.

- The inboard section on the wing was also refined in Grid H-D (4× in stream and 4× in span) and the grid points were redistributed in the spanwise direction to reduce the clustering at the wing-collar juncture and the wake of the chine vortex (see Fig. 2c). This redistribution was implemented for similar reasons that were highlighted in the previous item concerning the slat wake.

HRLES Grid H-D had approximately 571M grid points compared with 224M and 550M grid points for RANS Grids R-C and R-D, respectively. The corresponding Grid H-D wind tunnel mesh had 615M solve points.

IV. Results and Discussion

A. Results - Free Air Configuration

The HRLES results are compared with the QinetiQ experimental data as well as the corrected forces and moments for the full alpha sweep: $\alpha = 7.05°, 11.29°, 17.05°, 19.57°, 20.55°$ and $21.47°$. The flow conditions and geometry parameters for the CRM-HL simulations are provided in Table 2. The HRLES simulation results presented were initialized as *cold-starts*, unless otherwise noted, wherein the simulations for each angle-of-attack were initialized using a freestream condition (impulsive start). Statistical stationarity was established by assessing the load histories and time averaging of surface data and instantaneous loads was performed through an appropriate averaging window based on the longest time scale motions observed at each angle of attack. In practice, this required that at least 20-30 non-dimensional time units (tU_{ref}/c_{MAC}, where c_{MAC} is the mean aerodynamic chord) were simulated exclusively for temporal averaging for the majority of the simulated angles and over 50 CTUs used for the highest angle-of-attack.

Fig. 3 shows the time-averaged aerodynamic loads as a function of angle-of-attack for the various grids considered. All but one of the simulations presented were run with a fixed time-step size of 0.2ms (a non-dimensional timestep size of $1.94 \times 10^{-3} \Delta t U_{ref}/c_{MAC}$). The grid LES time-scales shown in Fig. 4 illustrate the validity of this choice for grid level H-D (at $\alpha = 21.47°$); the green regions highlight areas where the choice of time step respects the *resolvable* time scales while the red regions highlight areas where the local grid length scales permit existence of finer time-scale motions

Table 2   Freestream conditions and parameters for CRM-HL simulations.

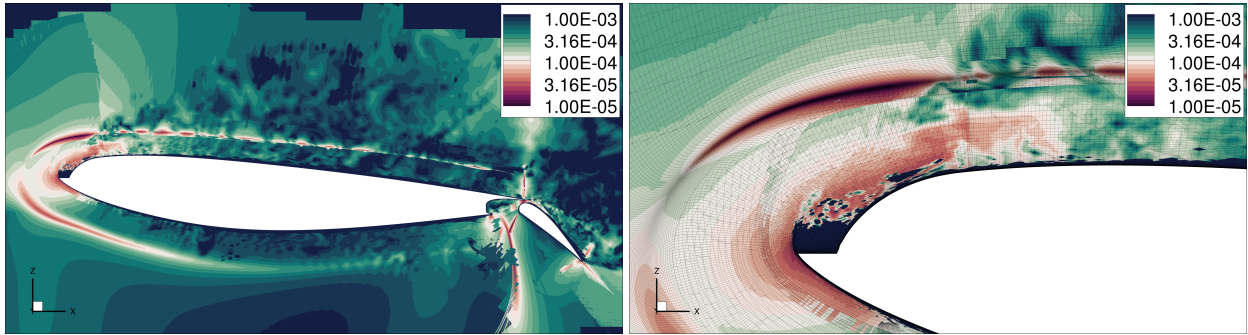| Condition	Value
Mean Aerodynamic Chord, c_{MAC} (m)	7.00532
Moment Reference Center (m)	(33.6779, 0.0, 4.51993)
Reference Area (m^2)	191.845
Mach Number, M	0.2
Reynolds Number, $\text{Re}_{c_{\text{MAC}}}$	5.49 M
Reference Static Temperature, T (K)	289.444
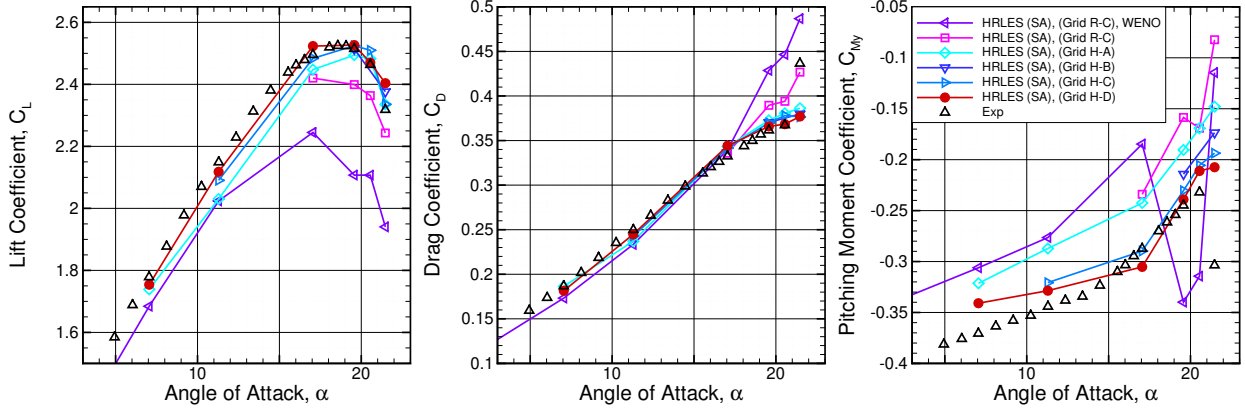
Fig. 3   Comparison of aerodynamic loads (C_L, C_D and C_{My}) for HRLES at various grid levels for the free air configuration.

(a) $y = 4.0$m slice

(b) $y = 4.0$m slice (zoomed in view)

Fig. 4   Grid time scales (based on an incompressible flow CFL condition of 1, local instantaneous velocity scale and grid scale). Note that the colormap is shown in exponential scale for $\Delta_T^{LES} = \Delta_T^{grid}/(f_d + \varepsilon)$ where the shielding function takes a value of 1 in LES mode and value of 0 in RANS mode; epsilon is a small float preventing a divide by zero. The flow field corresponds to an angle-of-attack of $21.47°$.

which are ultimately *filtered* by the BDF2 temporal discretization. It is evident that the majority of the resolvable LES motions are in-fact preserved by the time-step size, except near a small region near the leading edge close to the slat cutout. To test the temporal resolution requirement of hybrid RANS/LES simulations, an additional simulation was performed with a five time larger time-step size ($5\Delta t$) at the highest angles of attack. Several important observations can

be made regarding the choice of grids as well as the spatio-temporal discretizations employed:
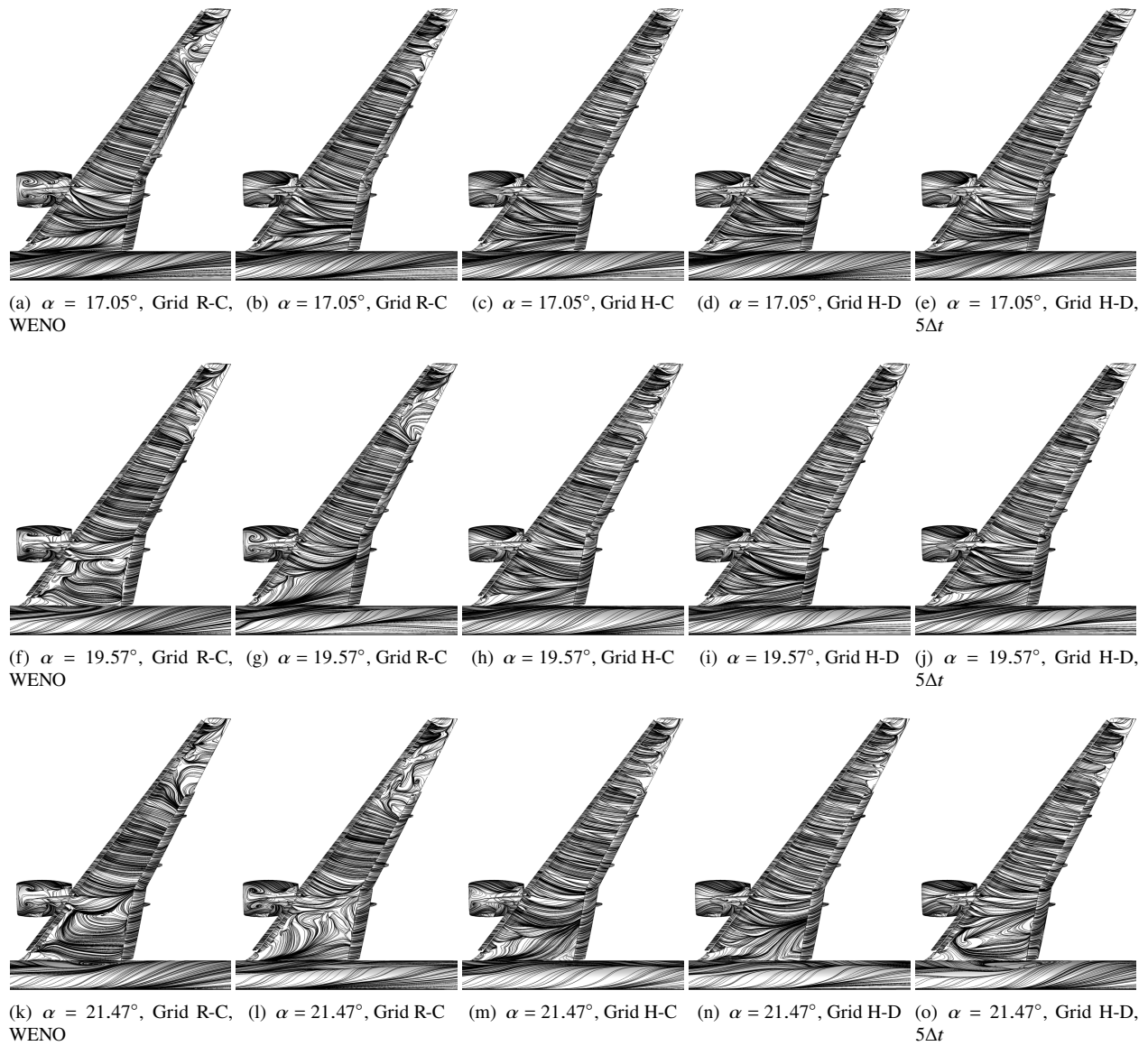

(a) α = 17.05°, Grid R-C, WENO (b) α = 17.05°, Grid R-C (c) α = 17.05°, Grid H-C (d) α = 17.05°, Grid H-D (e) α = 17.05°, Grid H-D, 5Δt

(f) α = 19.57°, Grid R-C, WENO (g) α = 19.57°, Grid R-C (h) α = 19.57°, Grid H-C (i) α = 19.57°, Grid H-D (j) α = 19.57°, Grid H-D, 5Δt

(k) α = 21.47°, Grid R-C, WENO (l) α = 21.47°, Grid R-C (m) α = 21.47°, Grid H-C (n) α = 21.47°, Grid H-D (o) α = 21.47°, Grid H-D, 5Δt

Fig. 5   Comparison of time averaged skin friction coefficient (c_f) **streamlines for obtained on various grid levels for HRLES showing the progression through** $C_{L,\mathbf{max}}$ **and stall.**

1) A large sensitivity is noted depending on the choice of grid employed for the hybrid RANS/LES simulations. The aerodynamic loads predicted by grid R-C regardless of the choice of numerical discretization imply a flow-field topology with excess/spurious outboard separation (see Fig. 5f,g), somewhat consistent with the RANS predictions at $C_{L,\mathrm{max}}$ with grids R-D (see Ref. [37]). The streamlines shown in Figs 5k,l also highlight a non-physical inboard flow topology showing large scale wing root separation resulting in pitch breaks that occur at either α = 17.05° (using WENO numerics) or at α = 20.55° (using less-dissipative numerics). However, post pitch break, the pitching moments show a nose-up tendency due to onset of large outboard separation which is
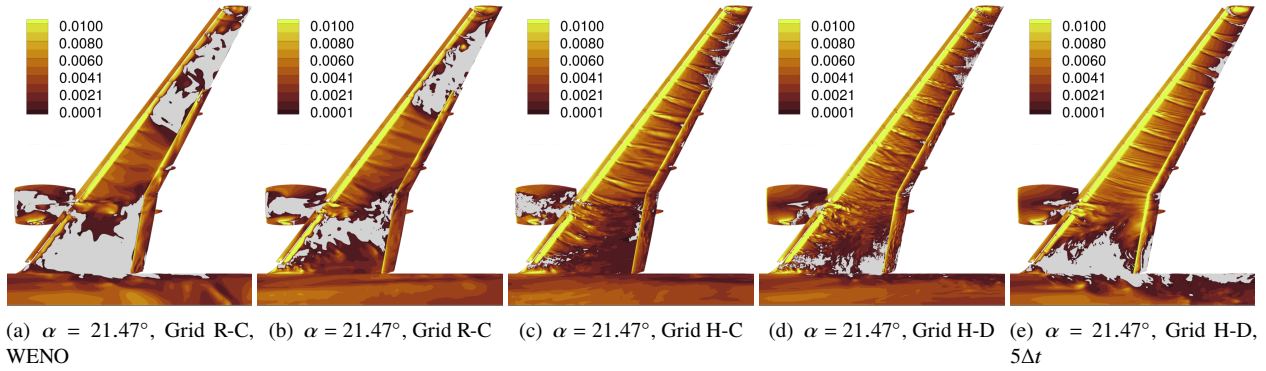
(a) α = 21.47°, Grid R-C, WENO   (b) α = 21.47°, Grid R-C   (c) α = 21.47°, Grid H-C   (d) α = 21.47°, Grid H-D   (e) α = 21.47°, Grid H-D, $5\Delta t$

Fig. 6   Instantaneous x−component of surface skin friction (c_{f_x}) obtained using HRLES at the α = 21.47° angle of attack in free-air configuration. The blanked regions depict negative (c_{f_x}) indicating regions of re-circulation.

unphysical and similar to steady-state RANS predictions. Overall HRLES solution accuracy on the grid R-C is inferior to that obtained using steady state RANS at all angles of attack studied, without exception (see Ref. [13, 37]). The grid-changes (discussed in Section III) that lead to grid H-D show a striking improvement in the overall solution quality. Upon inspection of the flow-field (including C_p profiles at $\eta = 0.82$ and $\eta = 0.91$ shown in Fig. 7), it is evident that the slat wake, which is now treated in LES mode supporting resolvable fluctuations that energize the main-element boundary layers prevents early onset of smooth body separation observed in RANS and for grid R-C HRLES. It is also observed that the integrated aerodynamic loads of lift and drag appear to converge, with increasing grid resolution, more rapidly than the pitching moment coefficient (see Fig. 3) which outlines the importance of obtaining grid convergence across all three aerodynamic coefficients. At this stage, it is also important to emphasize the need to refine in the spanwise/streamwise directions on the outboard wing - the spanwise and streamwise resolutions on grid H-D are approximately 8 and 16 times finer respectively than those used on the RANS grid R-C. Additionally, it is observed that for progressive inboard refinements - Grid R-C $\rightarrow$ Grid H-C $\rightarrow$ Grid H-D - and, particularly, for the post-stall angle-of-attack, $\alpha = 21.47°$, that (a) the separation near the wing/slat cutout region is reduced as seen in the time-averaged streamlines in Fig. 5l-n and (b) the inboard separation aft of the nacelle (Fig. 6b and Fig. 5l) is largely reattached (Fig. 6c and Fig. 5m) resulting in the developement of wing-root incipient corner-flow separation (Fig. 6d and Fig. 5n).

2) A second sensitivity to HRLES predictions that was explored using the RANS grid R-C was regarding the choice of the inviscid flux discretization. Two choices for midpoint right/left state interpolations were employed: a) WENO-JS [38] which acts as a limiter, and b) purely 4th order central interpolations which results in a non-dissipative discretization (see Sec. II.B). The CL predictions shown in Figure 3, highlight the strong sensitivity to numerical discretization observed around the $C_{L,\max}$ state. This is also very evident in both the surface streamlines (see for example the differences in the inboard and outboard flow topology at $\alpha = 19.57°$ in
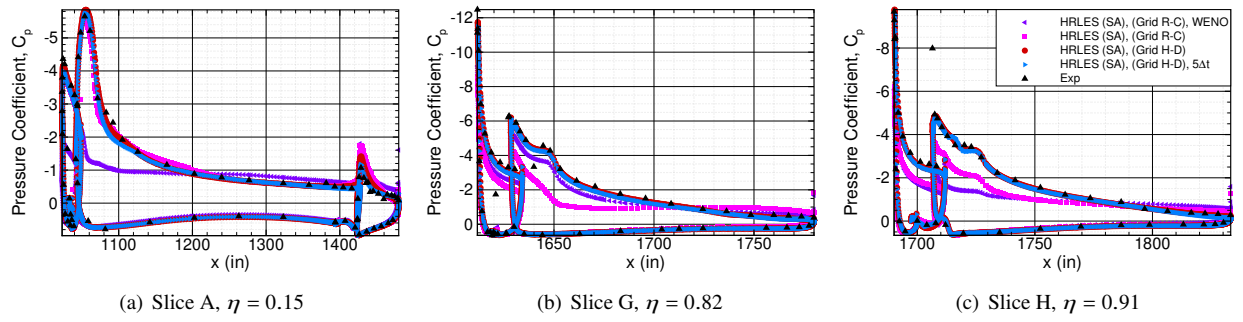
(a) Slice A, $\eta = 0.15$ (b) Slice G, $\eta = 0.82$ (c) Slice H, $\eta = 0.91$

Fig. 7 **Variations in surface pressure coefficient (C_p) slices for HRLES computed on various grid levels and timestep sizes at slices A, G and H (see Fig. 1) at $\alpha = 19.57°$.**
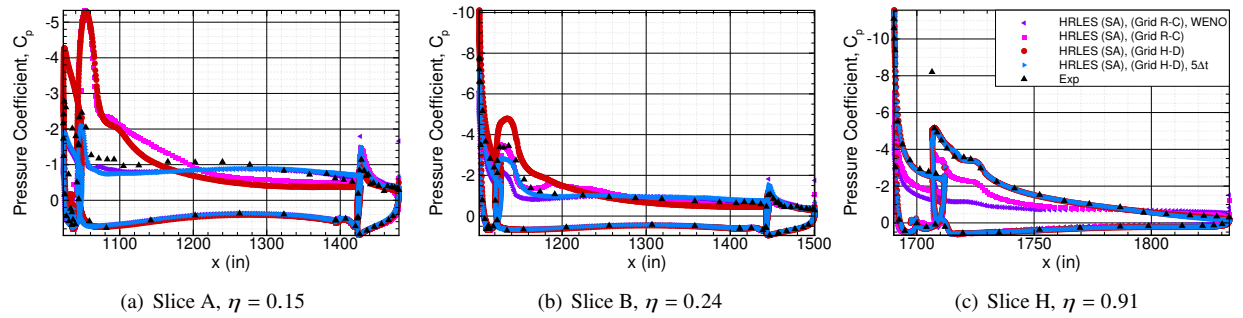

(a) Slice A, $\eta = 0.15$ (b) Slice B, $\eta = 0.24$ (c) Slice H, $\eta = 0.91$

Fig. 8 **Variations in surface pressure coefficient (C_p) slices for HRLES computed on various grid levels and timestep sizes at slices A, B and H (see Fig. 1) at $\alpha = 21.47°$.**

Fig. 5f and g) and the sectional C_p profile shows in Fig. 7 where the use of the dissipative WENO discretization results in large-scale spurious wing-root separation that is largely mitigated by the use of a central non-dissipative discretization for the inviscid flux on an identical grid (grid level R-C).

3) Next, the role of temporal discretization error introduced by the implicit BDF2 scheme is assessed. Note that increasing the time-step size results in (a) increase in temporal discretization error due to the BDF2 scheme itself, and (b) increase in SGS dissipation since the length scale used in the SGS closure may also be influenced by the time-step size as detailed previously. Thus the instantaneous surface skin friction in Fig. 6e shows this dissipative character when utilizing a large time-step size in scale resolving simulations. The aerodynamic loads predicted using the $5\Delta t$ only shows sensitivity at the highest angle-of-attack ($\alpha = 21.47°$) although a closer inspection of the surface flow at the $C_{L,\max}$ state (see Fig. 5i and j) does highlight some sensitivity near the slat cut-out that is largely consistent with the timescale observations made in Fig. 4. The most compelling difference however, occurs at the post $C_{L,\max}$ angle of attack $\alpha = 21.47°$. The large time step case shows a massive wing-root separation that appears to have grown from the slat cut-out region in contrast to the finer time-step baseline simulation which shows a growing corner-flow separation region. As a result, the large

time-step case also predicts an excessively large (compared to the experiment) pitch break, whereas the baseline simulation only shows a weak break in the pitching moment going from $\alpha = 20.55°$ to $\alpha = 21.47°$*.
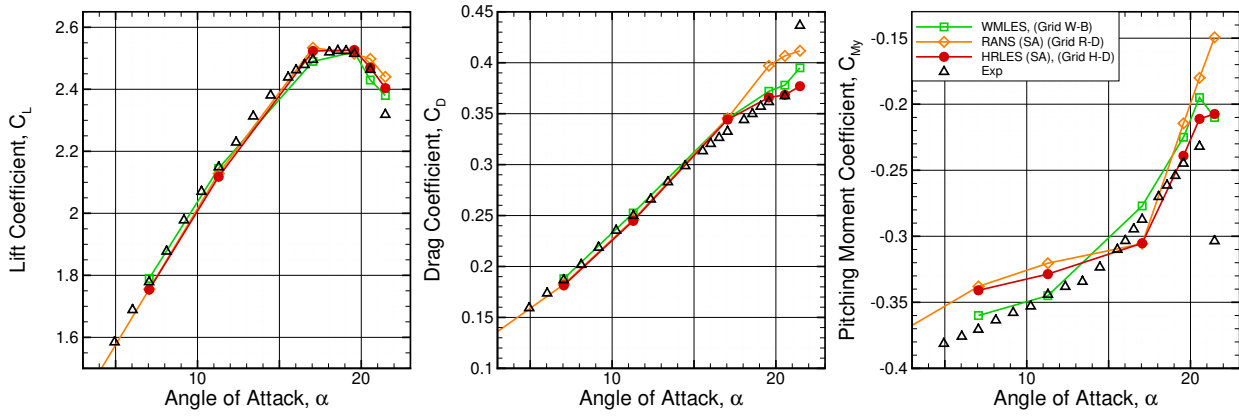

Fig. 9 **Comparison of aerodynamic loads (C_L, C_D and C_{My}) for RANS[13, 37], HRLES and WMLES[13, 39] for the free air configuration.**
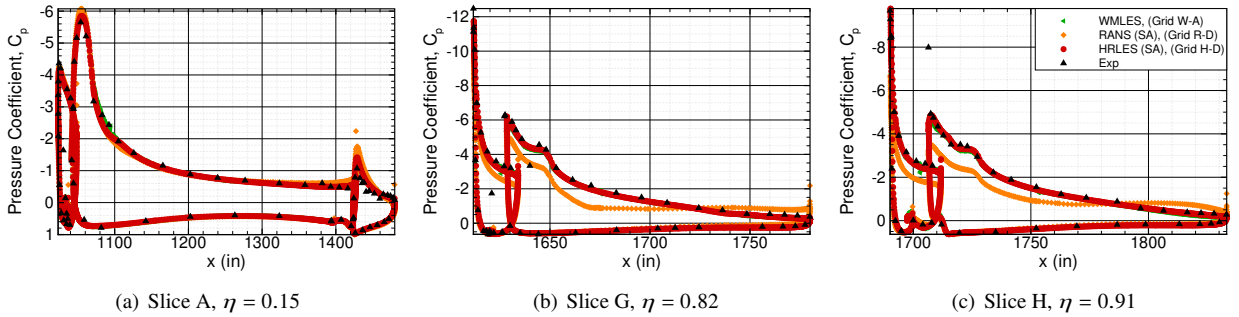

(a) Slice A, $\eta = 0.15$

(b) Slice G, $\eta = 0.82$

(c) Slice H, $\eta = 0.91$

Fig. 10 **Variations in surface pressure coefficient (C_p) slices for RANS[13, 37], HRLES and WMLES[13, 39] at slices A, G and H (see Fig. 1) at $\alpha = 19.57°$.**
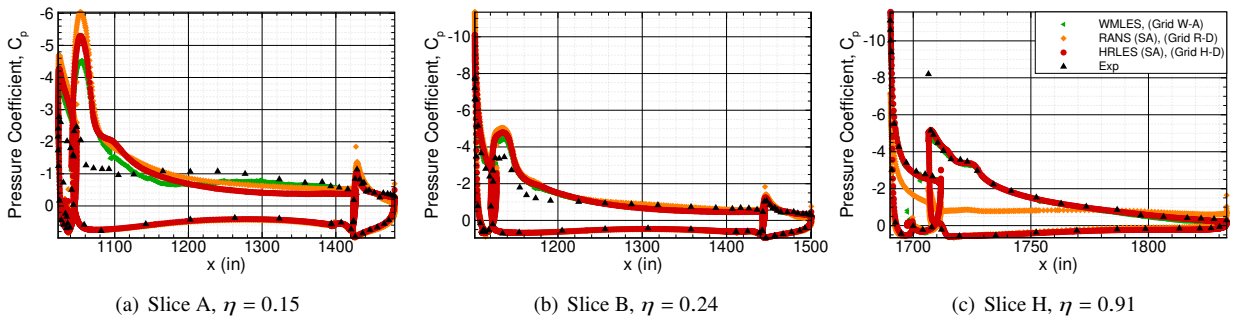

(a) Slice A, $\eta = 0.15$

(b) Slice B, $\eta = 0.24$

(c) Slice H, $\eta = 0.91$

Fig. 11 **Variations in surface pressure coefficient (C_p) slices for RANS[13, 37], HRLES and WMLES[13, 39] at slices A, B and H (see Fig. 1) at $\alpha = 21.47°$.**

---

*The word *pitch-break* is used herein to identify changes to the pitching moment slope, i.e., $\frac{\partial cm}{\partial \alpha}$ as opposed to a rise or drop in the pitching moment coefficient itself.
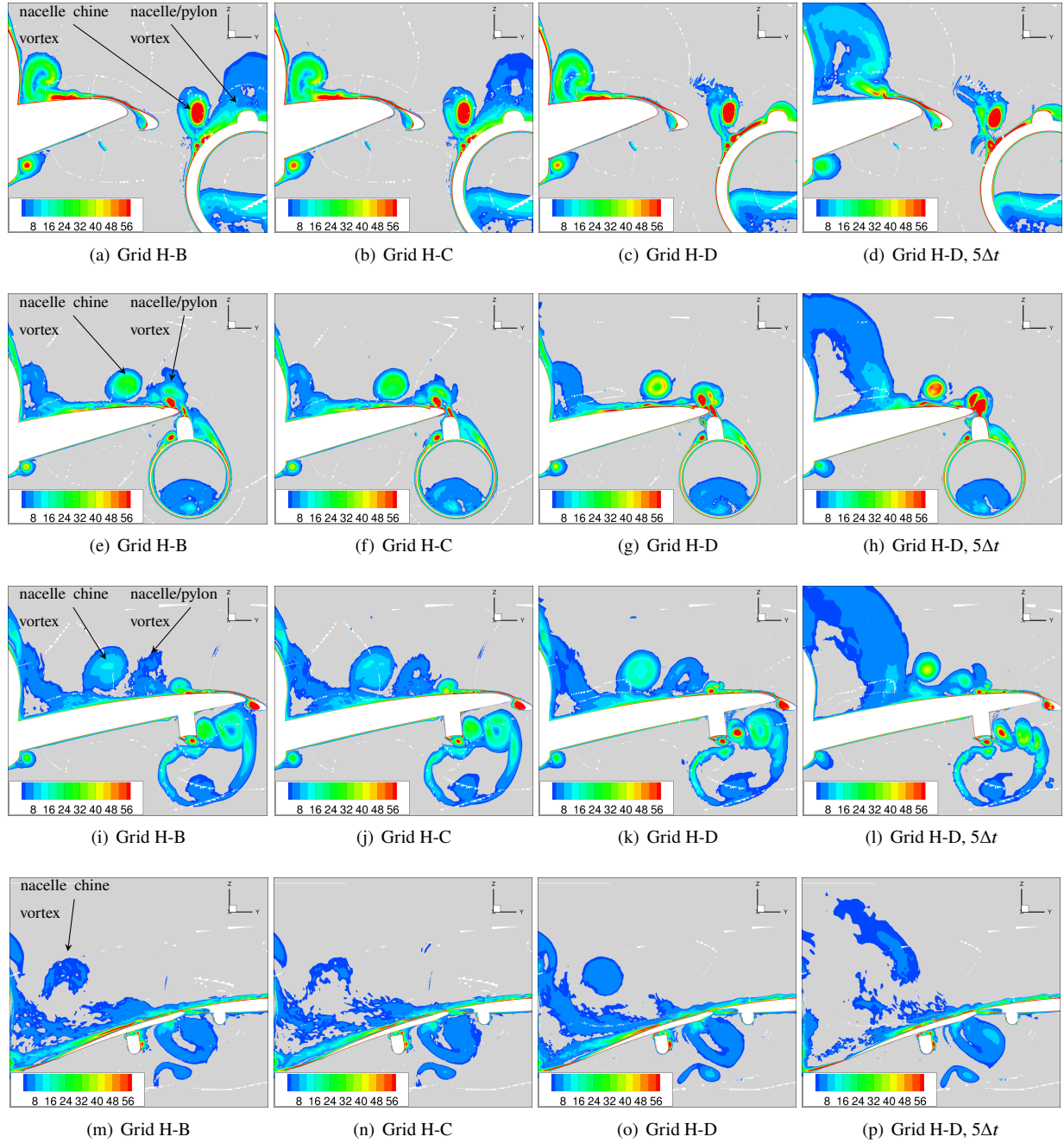
Fig. 12 **Vorticity magnitude corresponding to the time averaged solution for various grid levels and timestep size shown on the plane at** $x = 27.81m$ **(first row),** $x = 30.1m$ **(second row),** $x = 32.38m$ **(third row), and** $x = 37.72m$ **(fouth row) (see Fig. 1 for locations of slices on CRM-HL) with HRLES at the free air configuration post-stall angle-of-attack,** $\alpha = 21.47°$. **Vorticity field has been non-dimensionalized using the reference chord,** c_{MAC} **and the reference freestream velocity,** u_{ref}.

4) The best practice HRLES results are compared with LAVA RANS[13, 37] and WMLES[13, 39] best practice

   results for the CRM-HL in the free air configuration. The RANS simulations are on Grid R-D with the same SA

   closure and the WMLES simulations were performed on grid W-B with an algebraic equilibrium wall-function

14

(see individual papers for more details). Considering the comparison of the aerodynamic loads in Fig. 9, HRLES shows good agreement with WMLES and both scale resolving simulations provide a substantial improvement in $C_{L,\max}$ predictions when considering the surface pressure coefficients at $\alpha = 19.57°$ (see Fig. 10). Although RANS seems to provide an accurate C_L at $\alpha = 19.57°$, this appears to be as a result of error-cancellation, namely: the underprediction of suction on the outboard wing being compensated for by an overprediction of wing-root suction. At the post-stall angle-of-attack, $\alpha = 21.47°$, the outboard region of the wing has completely separated in the RANS solution in slices G and H Fig. 11b,c. It can be seen that HRLES is able to address this excessive outboard wing separation and give a superior prediction of the outboard flow. Furthermore, as a result of failing to correctly capture the outboard flow, RANS does not predict a pitch break between the two highest angles-of-attack in contrast to the scale resolving simulations (see Fig. 9).

5) A comparison study of the CRM-HL with and without the chine attached to the nacelle showed a marked difference in the inboard flow topology[40]. The chine vortex was shown to reduce the growth of the low-pressure region on the main wing and help prevent separation associated with the nacelle/pylon vortex, but may cause wing-root separation at the post-stall angle-of-attack[40]. Fig. 12 shows the progression of the nacelle chine and nacelle/pylon vortices along the CRM-HL for various grid levels and time-step sizes with HRLES at the post-stall angle-of-attack, $\alpha = 21.47°$. Interestingly, there seems to be a strong correlation between the intensity of the chine vortex on the main element and the strength of the pitch break observed in the pitching moment coefficient (see Fig. 3 and 13). This correlation also manifests itself in the progression of inboard separation observed: Grid H-B (no separation, not shown), Grid H-C (no separation, see Fig. 5m), Grid H-D (incipient corner-flow separation, see Fig. 5n) and Grid H-D, $5\Delta t$ (fully-formed separation, see Fig. 5o).
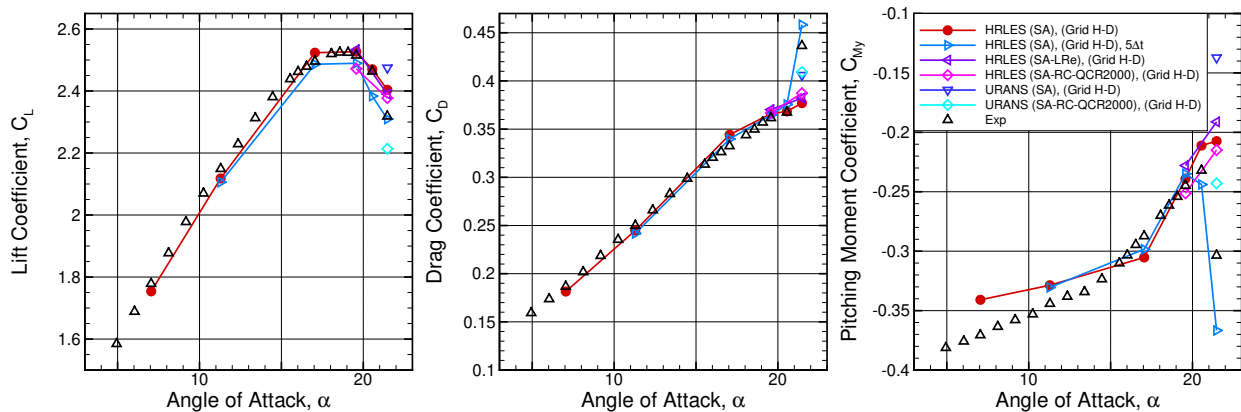

Fig. 13   Comparison of aerodynamic loads (C_L, C_D and C_{My}) for URANS and HRLES for various RANS closure models for the free air configuration.

6) Next, the sensitivity of the HRLES solution in the free air configuration to the underlying RANS closure model employed, is evaluated. Simulations at $C_{L,\max}$, $\alpha = 19.57°$, and $\alpha = 21.47°$ for SA-LRe (low Reynolds number

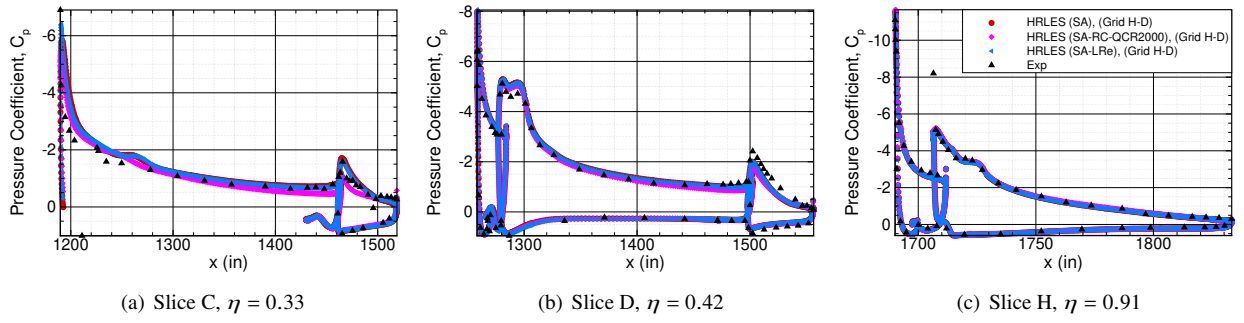(a) Slice C, $\eta = 0.33$ (b) Slice D, $\eta = 0.42$ (c) Slice H, $\eta = 0.91$

Fig. 14 Variations in surface pressure coefficient (C_p) slices for HRLES computed on various RANS closures at slices C, D and H (see Fig. 1) at $\alpha = 21.47°$.
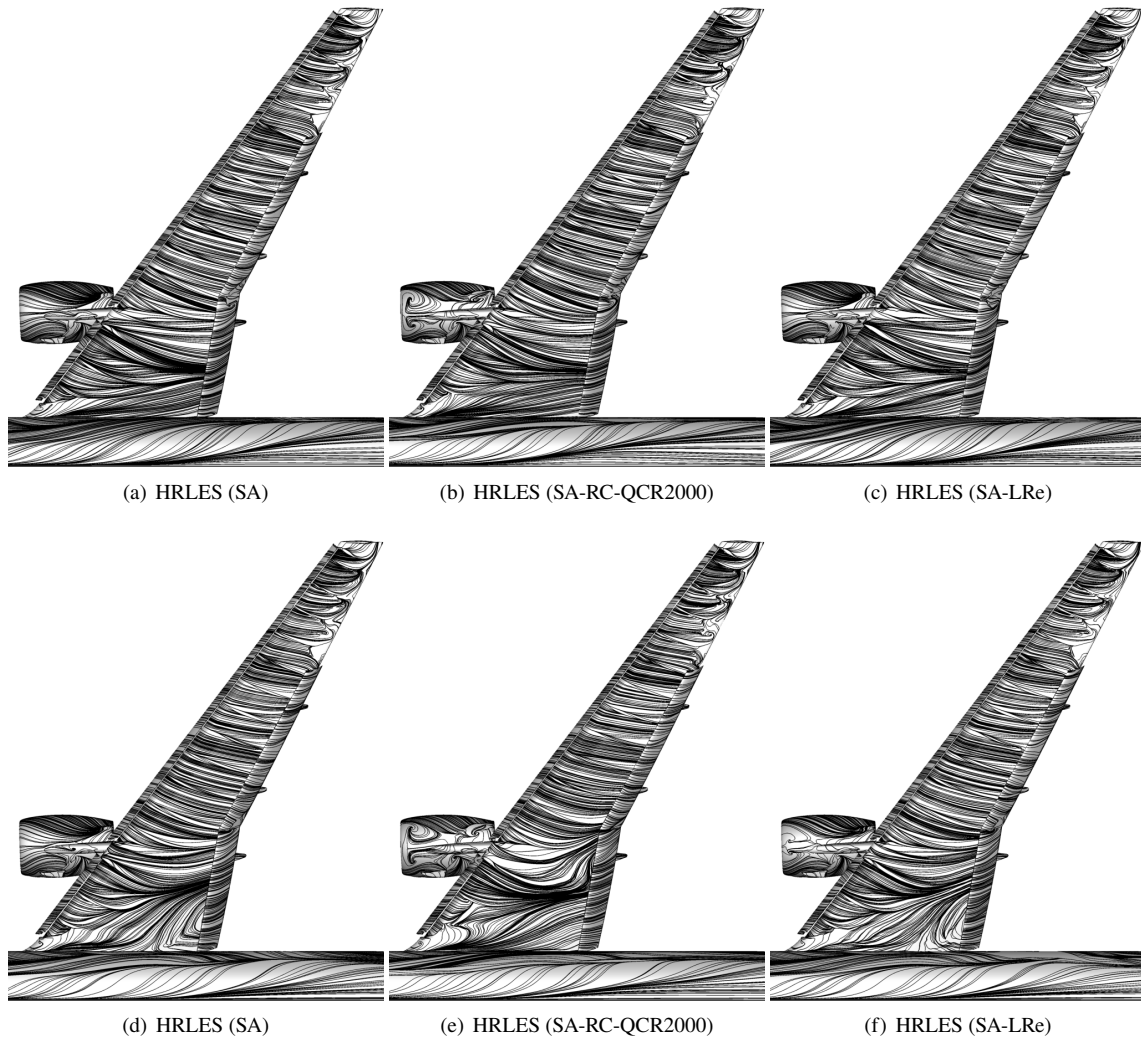

(a) HRLES (SA)   (b) HRLES (SA-RC-QCR2000)   (c) HRLES (SA-LRe)

(d) HRLES (SA)   (e) HRLES (SA-RC-QCR2000)   (f) HRLES (SA-LRe)

Fig. 15 Comparison of time averaged skin friction coefficient (c_f) streamlines for HRLES on Grid H-D for various RANS closures at $C_{L,\text{max}}$, $\alpha = 19.57°$, (upper row) and post-stall, $21.47°$, (lower row).

(a) HRLES (SA)
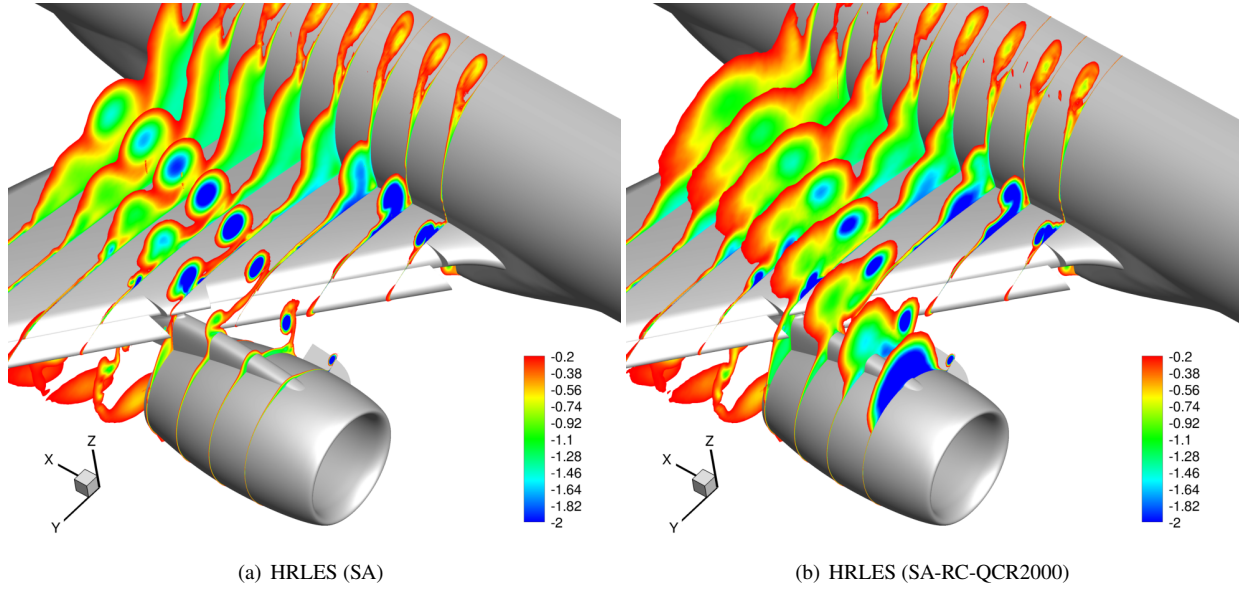
(b) HRLES (SA-RC-QCR2000)

Fig. 16 $C_{p,t}$ **contours showing total pressure deficit for the free air configuration at** $\alpha = 21.47°$ **with HRLES (SA) and (SA-RC-QCR2000).**

correction) and SA-RC-QCR2000 (Rotation Curvature/Quadratic Constitutive Relation) were run by initializing from the SA only solution at the same angle-of-attack, rather than from a freestream initial condition. The SA-RC-QCR2000 model shows a small drop in lift at $C_{L,\mathrm{max}}$ and there is also a spread in values of pitching moment coefficient, at $\alpha = 21.47°$, predicted when comparing the three closures (see Fig. 13). Very similar flow topologies are seen at $C_{L,\mathrm{max}}$ for the three closures in Fig. 15 with the main difference being that the flow becomes separated on the nacelle for SA-RC-QCR2000. At $\alpha = 21.47°$, there is a considerable difference in the flow topology visible on the inboard section of the wing between SA/SA-LRe and SA-RC-QCR2000, namely: the HRLES with SA/SA-LRe shows incipient corner-flow separation, while SA-RC-QCR2000 does not. In addition, SA-RC-QCR2000 also shows a different flow topology aft of the nacelle. The underprediction in the surface pressure coefficient for SA-RC-QCR2000 on slices C and D, towards the trailing edge of the main wing, in Fig. 14 may be a result of the flow separation seen on the nacelle. Further evidence of the two different flow topologies obtained with SA and SA-RC-QCR2000 closure models for HRLES is provided in Fig. 16 where contours of stagnation pressure coefficient, C_{pt}, are shown at different streamwise locations along the CRM-HL at 21.47°. It can be seen that the separated nacelle in Fig. 16 leads to a weakening of the chine vortex along the wing which also coincides with a larger nacelle/pylon vortex which results in a large pressure deficit downstream of the nacelle. The total pressure deficit along the wing-fuselage juncture appears to increase in Fig. 16a which may lead to the corner-flow separation seen in Fig. 15d. These results suggest the behaviour of the nacelle chine and nacelle/pylon vortex are closely linked to whether or not corner-flow separation develops at the post-stall

angle-of-attack. Importantly, it appears that regardless of the improvements by [20] to improving shielding function there still remains large sensitivities to the underlying closure.

B. Results - Wind Tunnel Configuration

1. Tunnel Initialization Procedure

The initialization procedure and HRLES simulation approach for the wind tunnel configuration of the CRM-HL are outlined. To obtain the desired reference Mach and Reynolds number in the tunnel test section, steady-state RANS (SA) simulations on Grid R-C are computed. Three different steady-state RANS solutions are evaluated for each angle-of-attack: the first and second with two different estimates for the back pressure and then a final run to confirm the calibrated back pressure, from run 1 and 2, gives the expected flow conditions (see Refs. [41–45]). Once the back pressure, that helps match the flow conditions measured in the test section, is obtained, the RANS solution is interpolated onto the wind tunnel grid system, Grid H-D, and used as an initial condition. It was noted by the authors in [13] that when performing scale resolving tunnel simulations, the test section Mach number began to drift slightly due to the absence of a closed loop controller for the back pressure. To reduce the tendency of this drift, the zones of the tunnel grid system that are off-body are fixed in RANS mode ($f_d = 0$). The near-body grids are handled with the mode 2 (automatic) shielding function approach. The free-air HRLES results were sensitive to the initial condition, particularly
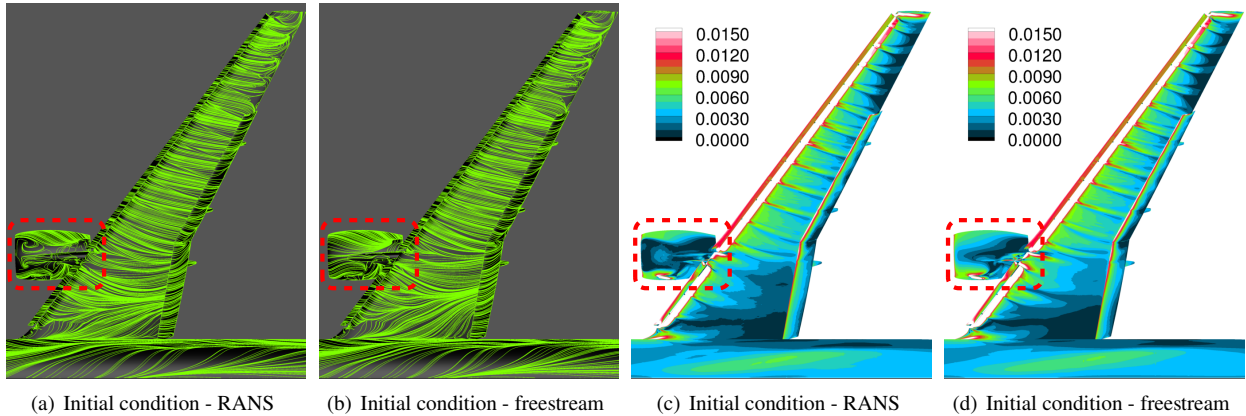

(a) Initial condition - RANS   (b) Initial condition - freestream   (c) Initial condition - RANS   (d) Initial condition - freestream

Fig. 17 Comparison of time averaged skin friction coefficient (c_f) streamlines (a),(b) and (c_f) contours (c),(d) for HRLES initializing from a steady state RANS solution and initializing from freestream on Grid H-D in the wind tunnel at $\alpha = 17.98°$. The red dashed line outlines the difference in flow topology on the nacelle.

on the nacelle around $C_{L,\max}$ and post-stall; namely, for the SA closure, significant flow separation occurred on the nacelle when initializing from a steady-state RANS solution whereas the flow remained attached when initializing from a *"cold-start"* (freestream). It is not clear if this is due to there being multiple solution branches or that the shielding function is not able to reattach the flow on the nacelle but is able to prevent separation from occurring when starting from freestream. Furthermore, it is also unclear if one or both solution branches exist in the limit $t \to \infty$. The same

sensitivity was observed for the tunnel simulations at $\alpha = 17.98°$ (see Fig. 17). Even with the noted differences of flow topology on the nacelle based on initial condition, only relatively weak downstream effects on the main element and flap are observed in Fig. 17. In order to mimic to the freestream initialization in the free-air case, the near-body grids are set to freestream values while the off-body grids are set to the interpolated RANS solution values. The advantage of using the RANS solution for the off-body grids is that it reduces the computational cost of *"washing out"* the initial transients and the calibrated back pressure established from the steady-state RANS runs can utilized.
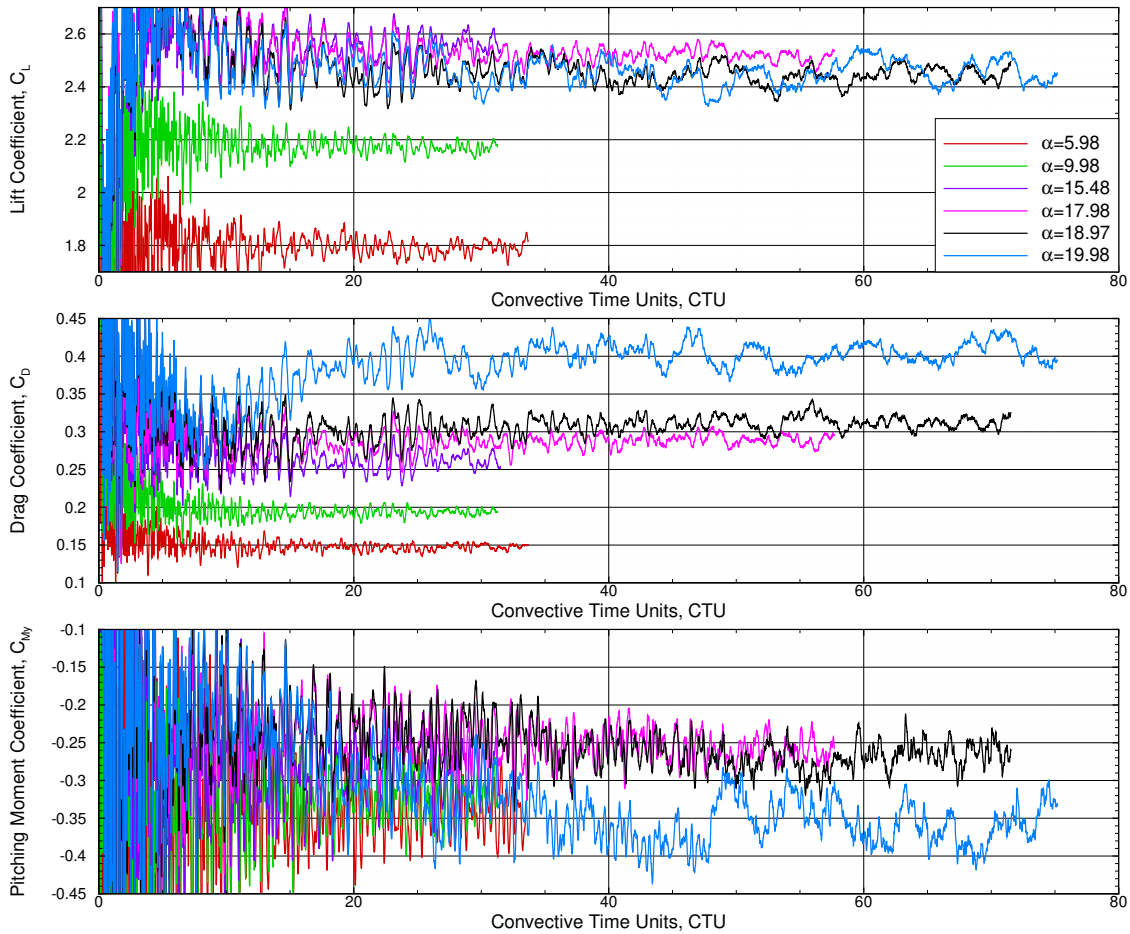
2. Results

Fig. 18   Aerodynamic loads histories (C_L, C_D and C_{My}) for HRLES on Grid H-D for the wind tunnel configuration at all angles in the alpha sweep.

HRLES wind tunnel simulations on Grid H-D for the full alpha sweep: $\alpha = 5.98°, 9.98°, 15.48°, 17.98°, 18.97°$ and $19.98°$ were performed. Fig. 18 shows the aerodynamic loads and pitching moment coefficients (C_L, C_D and C_{My}) histories for the HRLES wind tunnel simulations on Grid H-D for the full alpha sweep. It was noted that for the lower three angles-of-attack that approximately $30CTU$ was needed while $50 - 70CTU$ were required for the three higher

angles-of-attack. In particular, note that the pitching moment for the post-stall angle-of-attack, $\alpha = 19.98°$, shows a large standard deviation from the mean at 45 CTU which outlines the need to time integrate the simulations for a sufficiently long duration to obtain confidence in the *"stationarity"* of the solution. The solutions were time-averaged over the last $15 - 20CTU$ to obtain integrated loads, surface pressure and skin friction coefficients and these are compared with the uncorrected QinetiQ experimental data. The same near body grid system that was used in the free air case and the same time-step size (see Sec. IV.A). The following observations can be made regarding the HRLES results for the wind tunnel configuration:
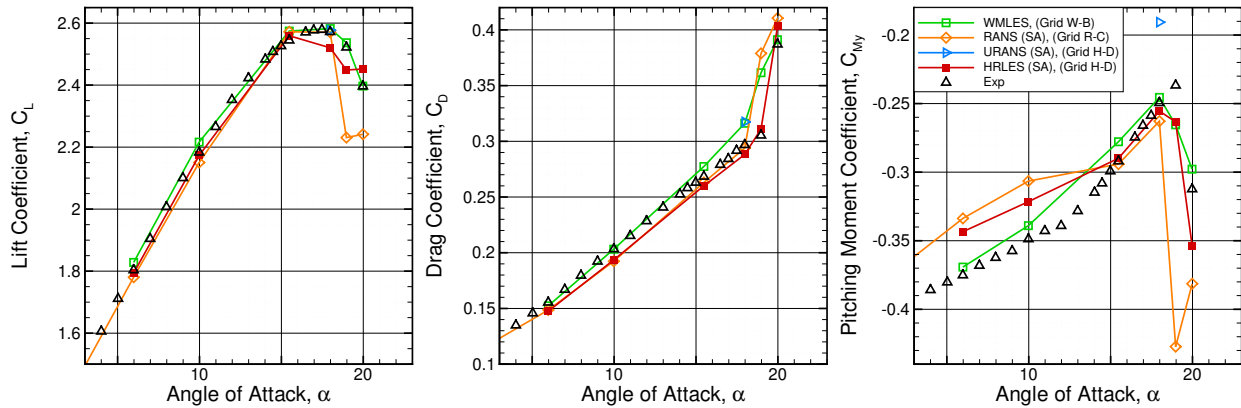

Fig. 19 Comparison of aerodynamic loads (C_L, C_D and C_{My}) for RANS[13, 37], HRLES and WMLES[13, 39] for the wind tunnel configuration.

1) Overall good agreement in the integrated loads is observed in Fig. 19 between the HRLES simulations and the experimental data. A slight under-prediction in lift is seen at $C_{L,\max}$ although the difference is quite small - HRLES predicted lift value differs by less than 2% from the experimental value - and meets the Certification by Analysis (CbA)[8] requirements. A strong pitch break is obtained post-$C_{L,\max}$ which is consistent with the experiment. However, the pitch break occurs one angle early with a weak break occurring between $\alpha = 17.98°$ and $\alpha = 18.97°$ and then subsequently a larger nose-down moment occurring at $\alpha = 19.98°$. This pitch break behaviour is also seen for both RANS (Grid R-C) and WMLES (Grid W-B) (see Fig. 19) although in the case of RANS, a massive pitch break is observed which corresponds to a sharp loss of lift at $\alpha = 18.97°$. It is clear that RANS fails to accurately predict the correct loads at the highest two angles-of-attack. The scale resolving (HRLES and WMLES) simulations also improve upon the RANS in the prediction of the pitching moment coefficient at low angles-of-attack. It may be that the higher nose-up pitching moment coefficient predicted by RANS and HRLES at $\alpha = 5.98°$ and $\alpha = 9.98°$ is due to an under-prediction in the surface pressure coefficient (C_p) on the suction side towards the trailing edge of the main element and the suction peaks on the outboard flaps (see slices D, E and F in Fig. 20c-e). A much closer agreement with the experiment is obtained on the suction peaks at the inboard flaps on slices B and C (see Fig. 20a-b) which may suggest the grid is under-resolved
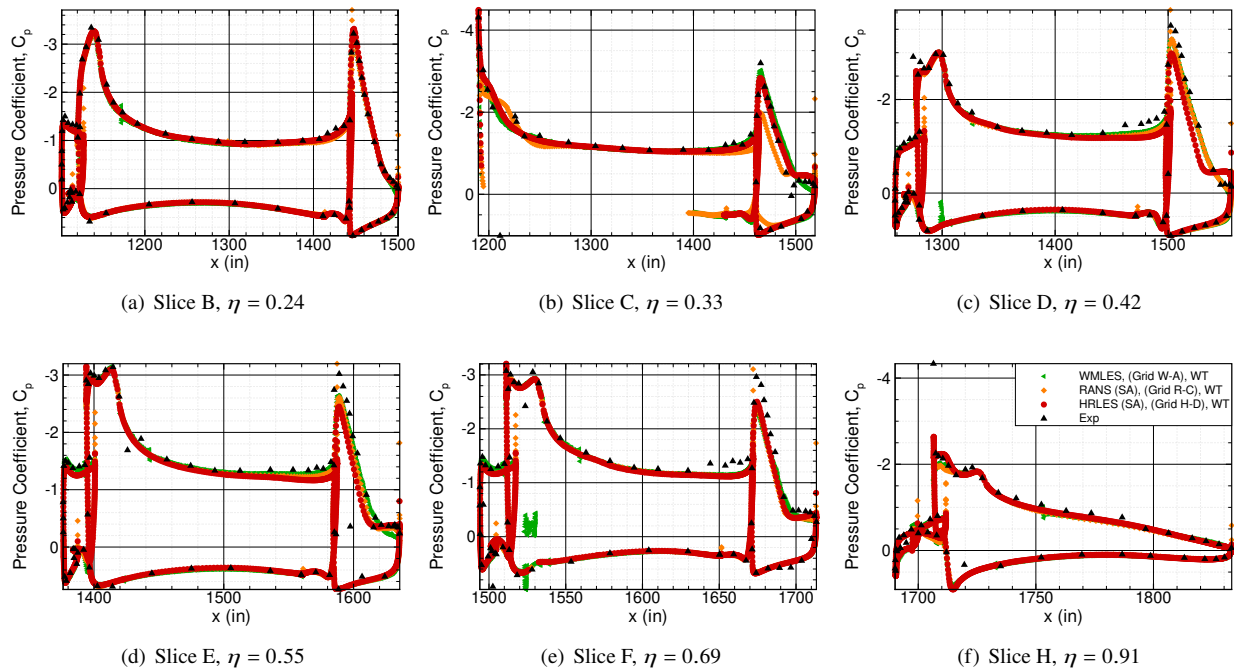
(a) Slice B, $\eta = 0.24$

(b) Slice C, $\eta = 0.33$

(c) Slice D, $\eta = 0.42$

(d) Slice E, $\eta = 0.55$

(e) Slice F, $\eta = 0.69$

(f) Slice H, $\eta = 0.91$

Fig. 20   Variations in surface pressure coefficient (C_p) slices for RANS[13, 37], HRLES and WMLES[13, 39] at slices B, C, D, E, F and H (see Fig. 1) at $\alpha = 5.98°$.

(a) Slice A, $\eta = 0.15$

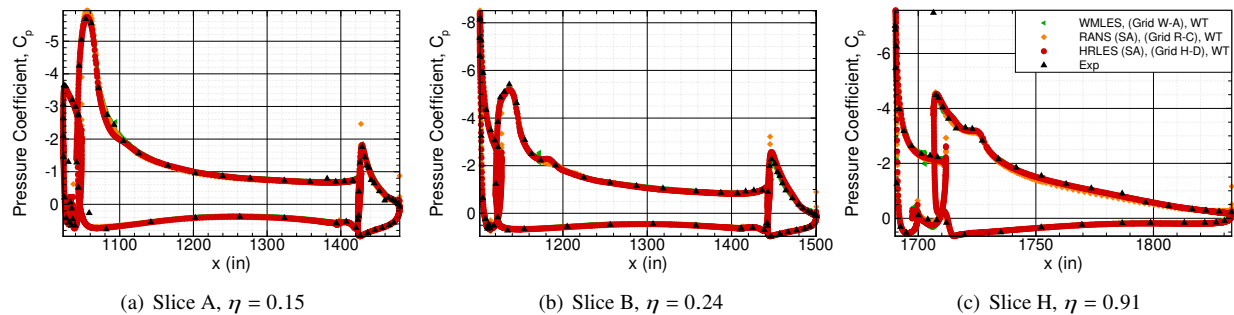(b) Slice B, $\eta = 0.24$

(c) Slice H, $\eta = 0.91$

Fig. 21   Variations in surface pressure coefficient (C_p) slices for RANS[13, 37], HRLES and WMLES[13, 39] at slices A, B and H (see Fig. 1) at $\alpha = 15.48°$.

on the midboard main element or outboard slats. Further analysis is given later when considering the oil-flow photographs from the QinetiQ tunnel. All three methods shows excellent agreement with the experimental C_p data at the pre-$C_{L,\max}$ angle of attack, $\alpha = 15.48°$, (see Fig. 21) - implying *"an accurate prediction, for the right reasons"*, for the loads and moments at this angle-of-attack. Both RANS and WMLES give a very slight over-prediction of the suction peak, on slice A, at $C_{L,\max}$ ($\alpha = 17.98°$), while HRLES shows excellent agreement at the peak (Fig. 22). However, the HRLES solution develops a *"kink"* in the pressure coefficient between $x = 1050in$ and $1100in$ on the suction side which is likely responsible for the slight under-prediction

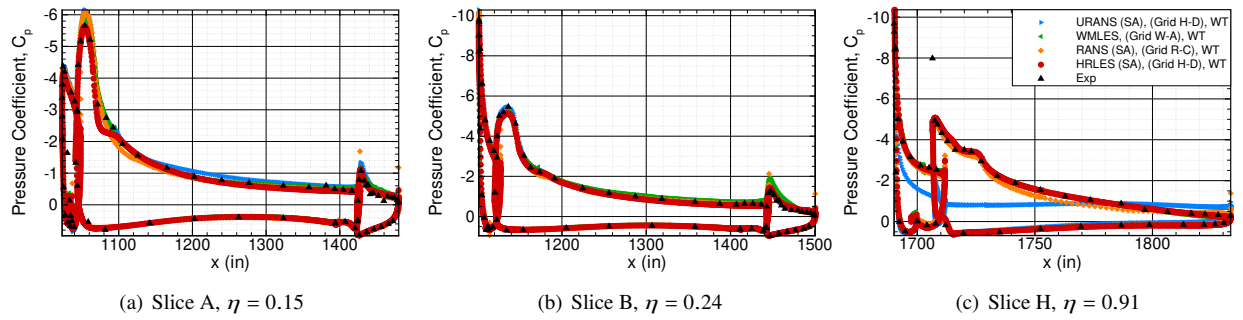(a) Slice A, $\eta = 0.15$ (b) Slice B, $\eta = 0.24$ (c) Slice H, $\eta = 0.91$

Fig. 22   Variations in surface pressure coefficient (C_p) slices for RANS[13, 37], HRLES and WMLES[13, 39] at slices A, B and H (see Fig. 1) at $\alpha = 17.98°$.

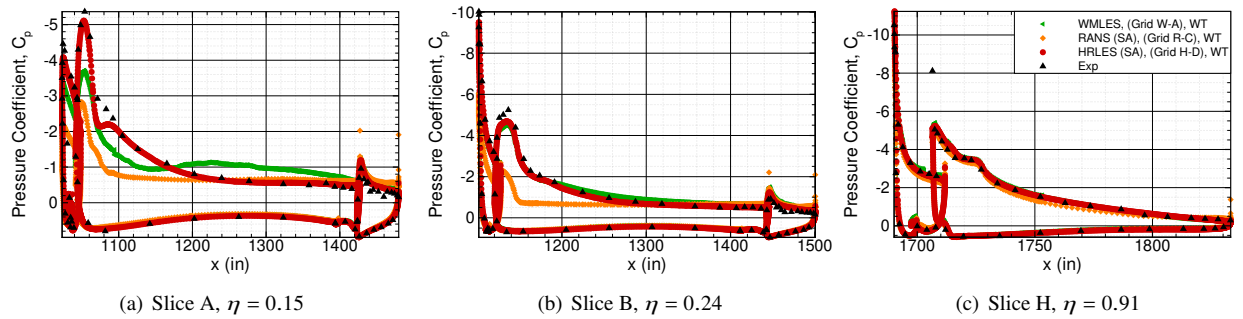(a) Slice A, $\eta = 0.15$ (b) Slice B, $\eta = 0.24$ (c) Slice H, $\eta = 0.91$

Fig. 23   Variations in surface pressure coefficient (C_p) slices for RANS[13, 37], HRLES and WMLES[13, 39] at slices A, B and H (see Fig. 1) at $\alpha = 18.97°$.

(a) Slice A, $\eta = 0.15$ (b) Slice B, $\eta = 0.24$ (c) Slice H, $\eta = 0.91$
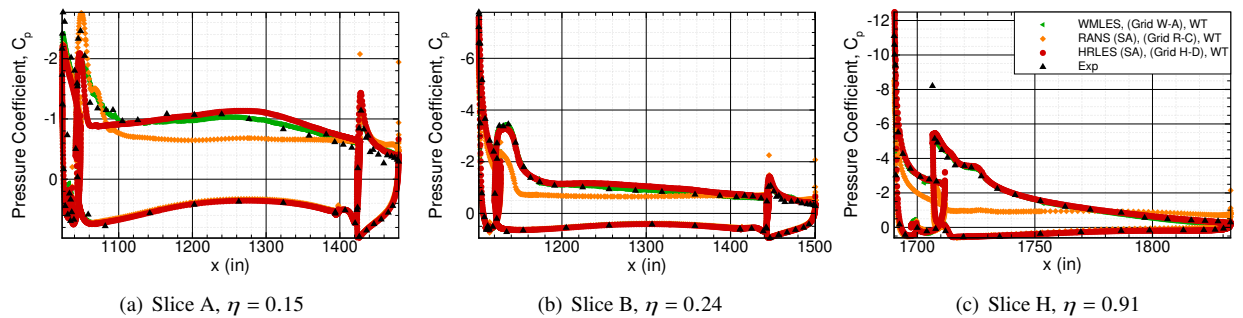
Fig. 24   Variations in surface pressure coefficient (C_p) slices for RANS[13, 37], HRLES and WMLES[13, 39] at slices A, B and H (see Fig. 1) at $\alpha = 19.98°$.

in the lift seen in Fig. 19. This *"kink"* persists through $\alpha = 18.97°$ (Fig. 23) and $\alpha = 19.98°$ (Fig. 24). Note that this region of the flow is located on the wing slightly downstream of the inboard wing/slat cutout and was previously highlighted in the discussion of the $C_{L,\mathrm{max}}$ case in the free air results in Sec. IV.A. Finer spatial or temporal resolution would be needed to establish whether this is due under-resolution or due to a local failure of the shielding function rather than the underlying RANS SA model closure. Next, it was shown for RANS (SA)

in the free-air case that when moving from Grid R-C to Grid R-D that the solution deteriorates outboard and massively separates in contrast to what was observed in the experiment. To confirm that this also occurs in the wind tunnel configuration, a URANS (SA) simulation was run conducted on Grid H-D and it was shown to have poorer agreement with experiment as a result of completely separating outboard (see Fig. 22c). Furthermore, the URANS (SA) simulation on Grid H-D predicted an inferior solution compared to the RANS (SA) solution on Grid R-C. At the next angle, $\alpha = 18.97°$, HRLES shows excellent agreement in the inboard slices A and B tracking the experimental surface pressure coefficient closely, particularly at the suction peaks (Fig. 23). Finally, both HRLES and WMLES show relatively good agreement with experiment at the highest angle-of-attack, $\alpha = 19.98°$, while RANS has completely separated inboard (Fig. 24a) and outboard (Fig. 24c).

2) The progression of the flow topology from $\alpha = 15.48°$ to $\alpha = 19.98°$ is shown in Fig. 25. No visible evidence of corner flow separation is seen at $\alpha = 15.48°$, incipient corner-flow separation can be visualized at $\alpha = 17.98°$ which then becomes progressively more fully formed separation at $\alpha = 18.97°$ and $\alpha = 19.98°$. The flow remains attached on the nacelle across the angles-of-attack and the flow topology outboard is consistent with the experiment (see Fig. 32). The streamlines are *"curling up"* into a vortex on the fuselage, at approximately half-chord, at $\alpha = 19.98°$ which is consistent with oil-flow photographs shown later in this paper. Interestingly, the skin friction coefficient streamlines for HRLES are more consistent with WMLES in the outboard region but more consistent with RANS in the inboard region at $C_{L,\max}$ (Fig. 26). However, at the post-stall angle-of-attack, $\alpha = 19.98°$ the scale resolving simulations show good agreement in the inboard flow topology whereas RANS is completely separated in the inboard region. Moreover, RANS shows a separated nacelle whereas the scale resolving simulations show predominately attached flow on the nacelles. All three methods show an apparent vortex at the Yehudi break along the boundary between the inboard and outboard flaps at $C_{L,\max}$ which is consistent with oil-flow photographs (view not shown in paper, see Ref. [9, 16]). RANS then shows another separated region on the outboard flap at the location of the middle flap fairing.

3) Fig. 27 to 32 shows a comparison of skin friction coefficient streamlines computed with HRLES and oil-flow photographs from the QinetiQ experiment at $\alpha = 5.98°$, $\alpha = 17.98°$, $\alpha = 18.97°$ and $\alpha = 19.98°$[†]. At the low angle-of-attack, $\alpha = 5.98°$, the flow remains attached on the main wing but separation is observed on both inboard/outboard flaps which is of a similar nature for both HRLES and experiment. From a qualitative point of view, excellent agreement can be observed at $C_{L,\max}$ with particular attention drawn to the nacelle, pylon and main element of the wing. The streamlines appearing to belong to the wing/slat cutout and slat-bracket vortexes converge to a very similar location on the wing trailing edge. At the next angle-of-attack $\alpha = 18.97°$ the corner-flow separation seen in the HRLES solution looks to be at a more advanced stage when compared to

---

[†]Oil-flow photographs can be useful and enlightening but are considered to be a qualitative measure only, because of uncertainties related to effects of oil thickness, viscosity, drying time, *etc.*[9]
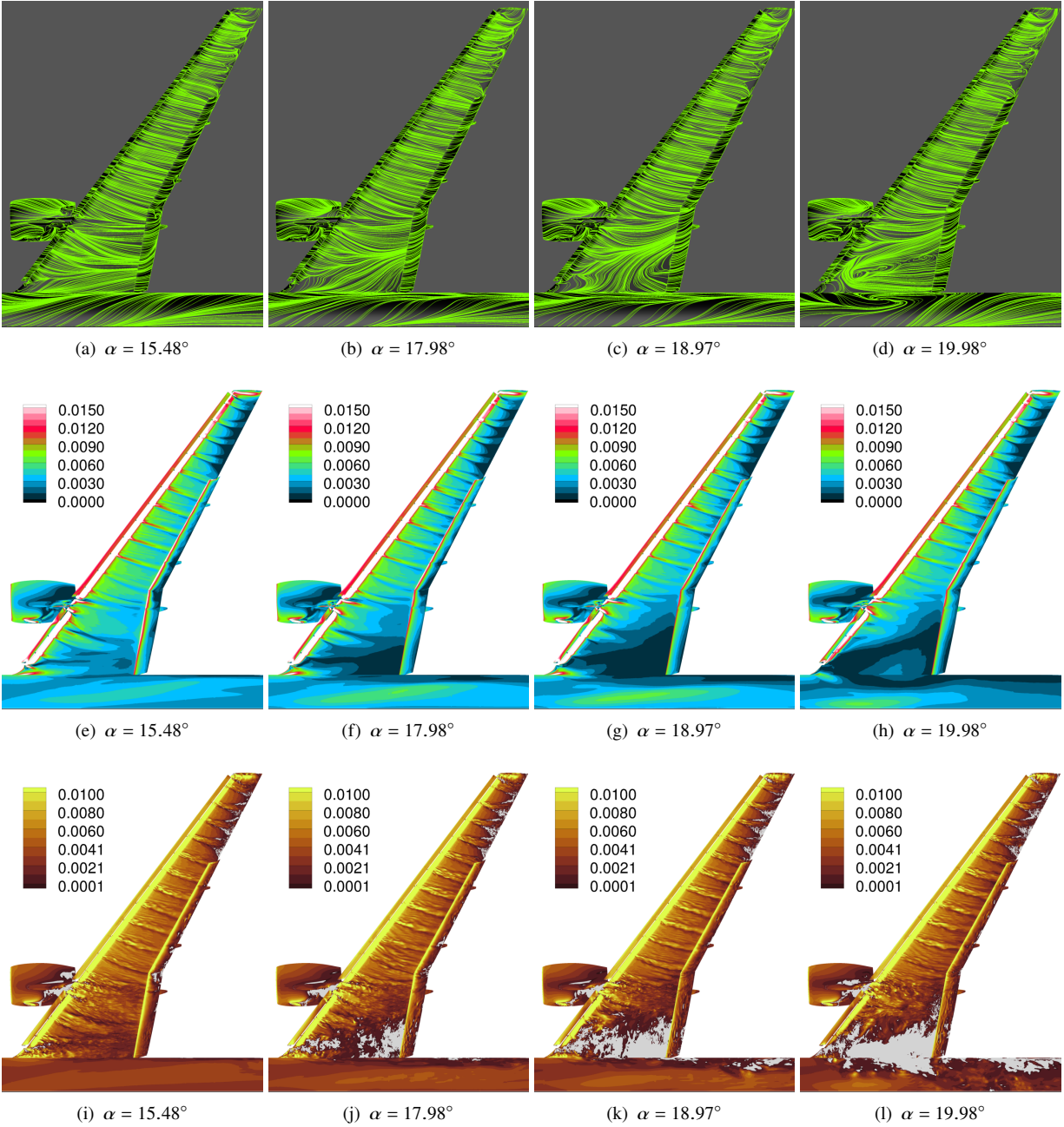
(a) $\alpha = 15.48°$ (b) $\alpha = 17.98°$ (c) $\alpha = 18.97°$ (d) $\alpha = 19.98°$

(e) $\alpha = 15.48°$ (f) $\alpha = 17.98°$ (g) $\alpha = 18.97°$ (h) $\alpha = 19.98°$

(i) $\alpha = 15.48°$ (j) $\alpha = 17.98°$ (k) $\alpha = 18.97°$ (l) $\alpha = 19.98°$

Fig. 25 **Comparison of time averaged skin friction coefficient** (c_f) **streamlines (upper),** c_f **contours (middle) and instantaneous** c_{f_x} **(lower) for HRLES on Grid H-D in the wind tunnel at the four highest angles:** $\alpha =$ $15.48°, 17.98°, 18.97°$ **and** $19.98°$**. The contour map is clipped for** $c_{f_x} < 0$ **to show regions of separated flow.**

the oil-flow. This is consistent with the pitch break at this angle-of-attack seen in Fig. 19. At the post-stalled angle-of-attack, $\alpha = 19.98°$, excellent agreement is observed in Fig. 30 and 31. Large wing-root separation can be visualized including a large fuselage vortex and a vortex located in the central part of the inboard region of the main element wing, both associated with separated flow. As previously mentioned, the flow topology
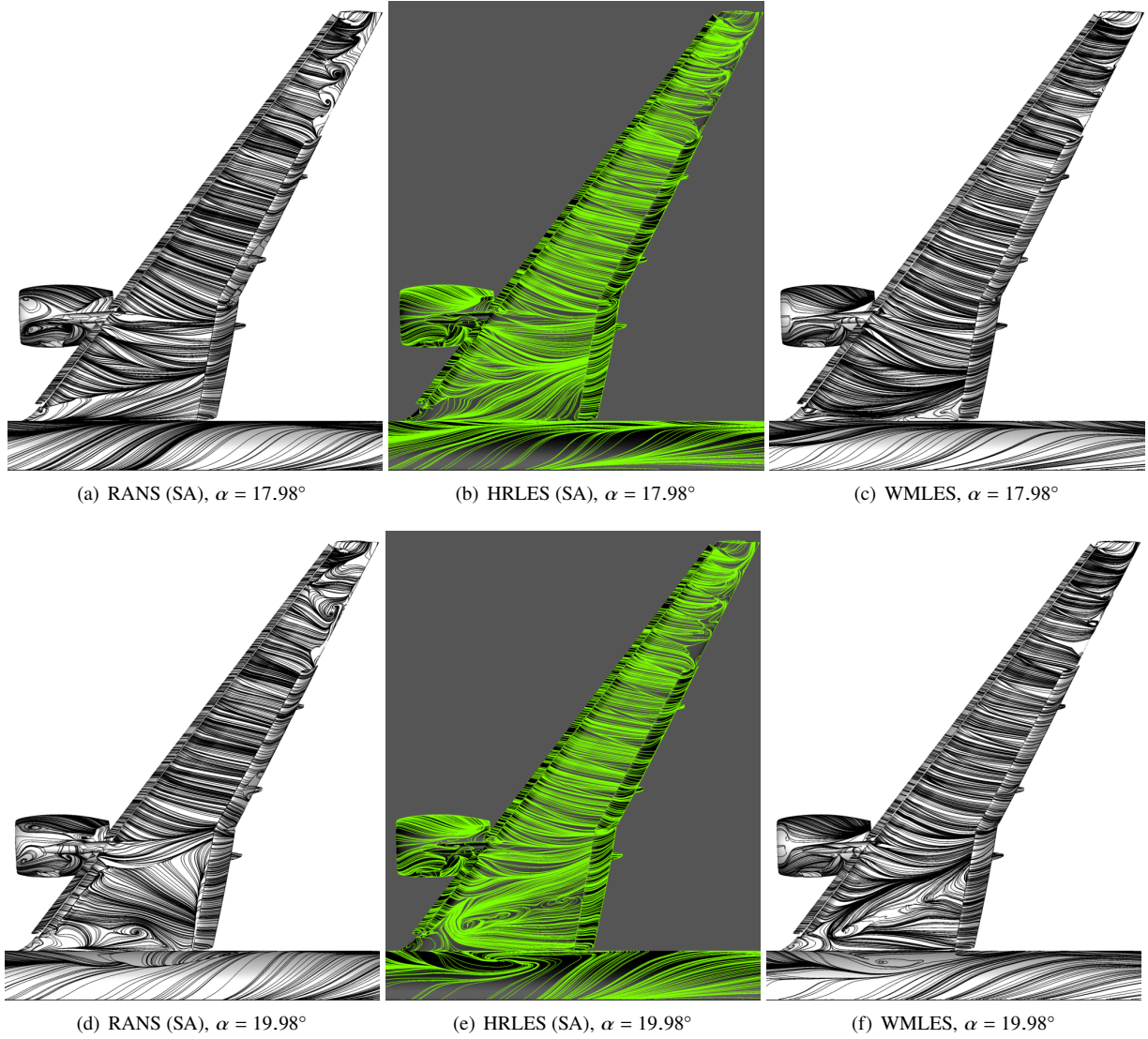
24

(a) RANS (SA), $\alpha = 17.98°$ (b) HRLES (SA), $\alpha = 17.98°$ (c) WMLES, $\alpha = 17.98°$

(d) RANS (SA), $\alpha = 19.98°$ (e) HRLES (SA), $\alpha = 19.98°$ (f) WMLES, $\alpha = 19.98°$

Fig. 26 Comparison of time averaged skin friction coefficient (c_f) streamlines for RANS[13, 37] (left), HRLES (center) and WMLES[13, 39] (right) in the wind tunnel at $\alpha = 17.98°$ and $\alpha = 19.98°$.

on the outboard region of the wing in the HRLES, which is dominated by the wakes of the slat-brackets and produces wedge-shaped flow structures, aligns well with the oil-flow photographs. This close agreement in the flow visualization is directly associated with the HRLES methodology, and related grid and shielding function improvements over RANS/URANS.
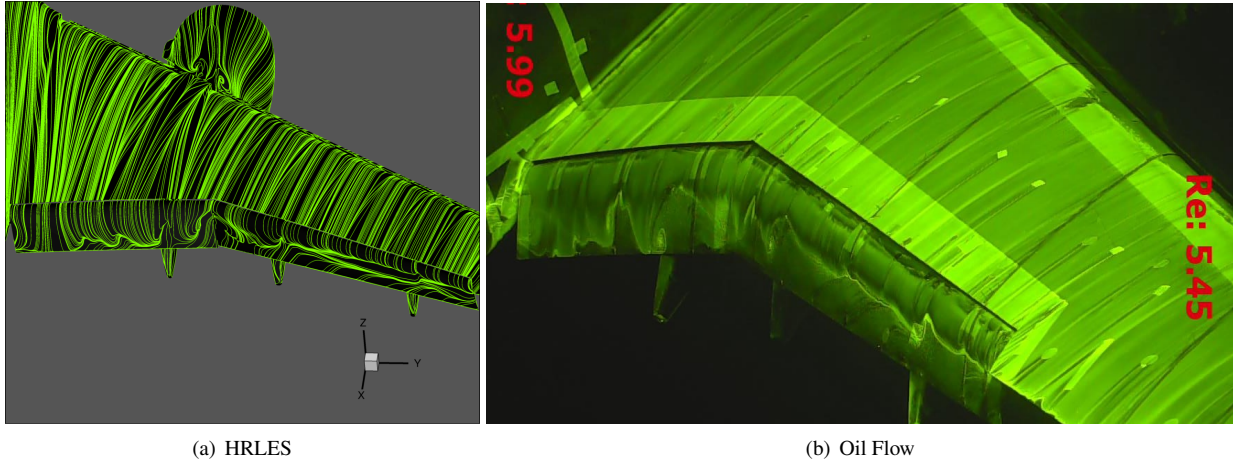
(a) HRLES

(b) Oil Flow

Fig. 27   Comparison of skin friction coefficient (c_f) streamlines from HRLES simulation on Grid H-D with oil flow photographs from the QinetiQ tunnel experiments[9, 16] (`https://hiliftpw.larc.nasa.gov`) at $\alpha = 5.98°$.

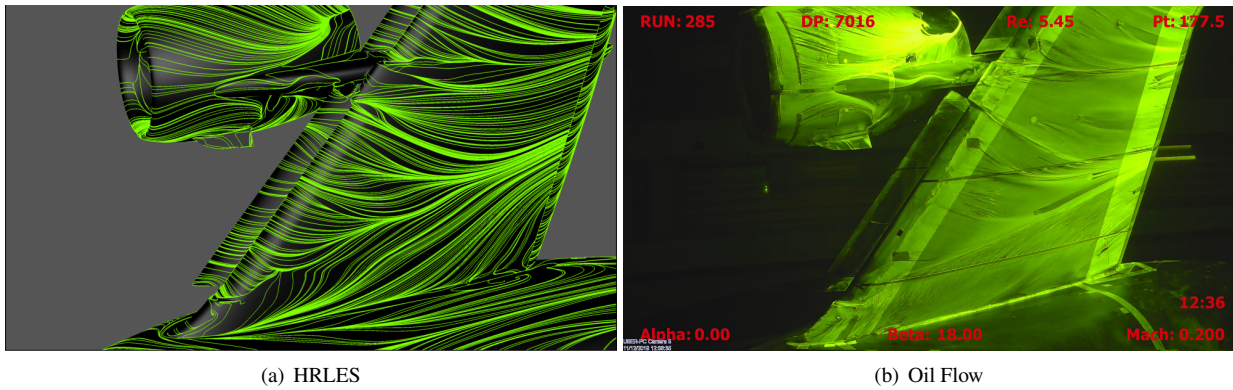
(a) HRLES

(b) Oil Flow

Fig. 28   Comparison of skin friction coefficient (c_f) streamlines from HRLES simulation on Grid H-D with oil flow photographs taken in the QinetiQ wind tunnel experiments[9, 16] (`https://hiliftpw.larc.nasa.gov`) at $C_{L,\mathbf{max}}$, $\alpha = 17.98°$ (approximately the same observer location).
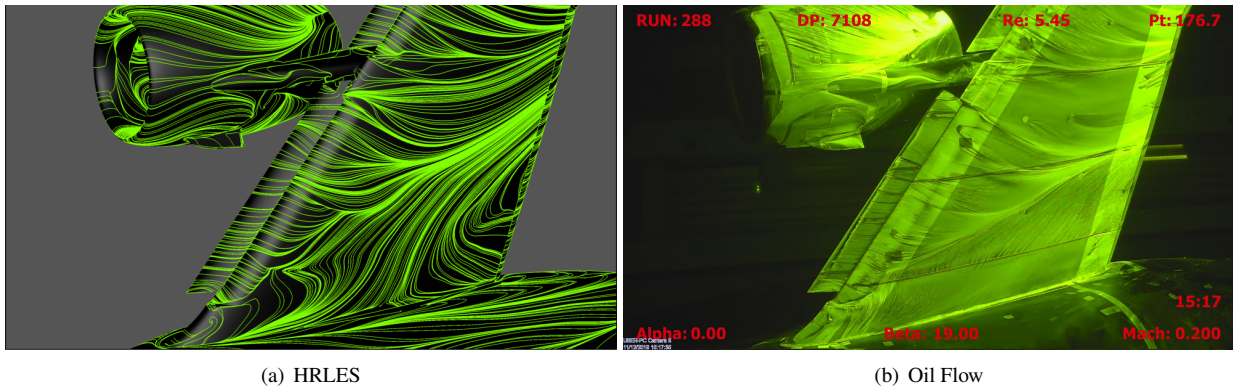

(a) HRLES

(b) Oil Flow

Fig. 29   Comparison of skin friction coefficient (c_f) streamlines from HRLES simulation on Grid H-D with oil flow photographs taken in the QinetiQ wind tunnel experiments[9, 16] (`https://hiliftpw.larc.nasa.gov`) at $\alpha = 18.97°$ (approximately the same observer location).
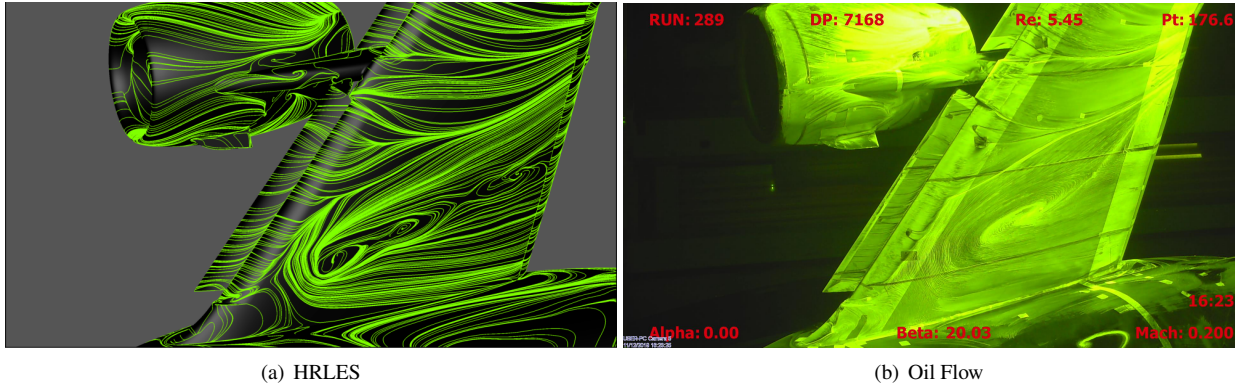
(a) HRLES

(b) Oil Flow

Fig. 30 **Comparison of skin friction coefficient (c_f) streamlines from HRLES simulation on Grid H-D with oil flow photographs taken in the QinetiQ wind tunnel experiments[9, 16] (`https://hiliftpw.larc.nasa.gov`) at a post-stall angle, $\alpha = 19.98°$ (approximately the same observer location).**

(a) HRLES

(b) Oil Flow

Fig. 31 **Comparison of skin friction coefficient (c_f) streamlines from HRLES simulation on Grid H-D with oil flow photographs taken in the QinetiQ wind tunnel experiments[9, 16] (`https://hiliftpw.larc.nasa.gov`) at a post-stall angle, $\alpha = 19.98°$. View of streamlines on the fuselage (approximately the same observer location).**
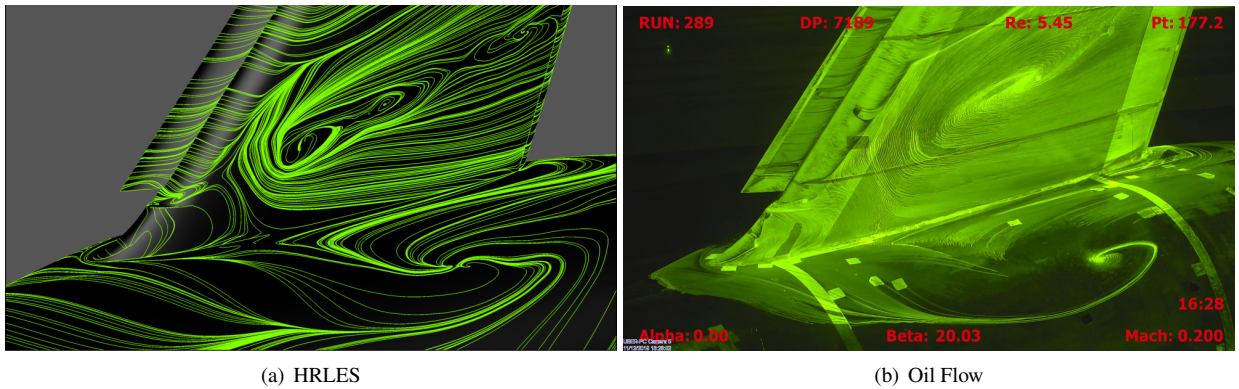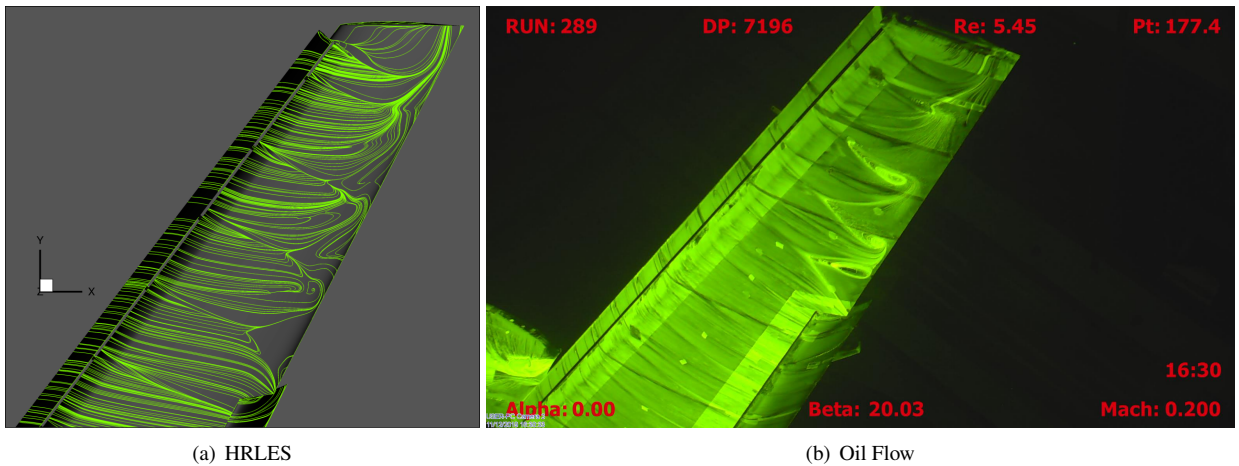

(a) HRLES

(b) Oil Flow

Fig. 32 **Comparison of skin friction coefficient (c_f) streamlines from HRLES simulation on Grid H-D with oil flow photographs taken in the QinetiQ wind tunnel experiments[9, 16] (`https://hiliftpw.larc.nasa.gov`) at a post-stall angle, $\alpha = 19.98°$. View showing streamlines on the outboard region of the wing.**

27

V. Conclusions

An assessment of a Hybrid RANS-LES (HRLES) approach for $C_{L,\max}$ and post-stall prediction of the NASA High-Lift Common Research Model (CRM-HL) or more broadly, an assessment of its applicability for $C_{L,\max}$ and post-stall prediction of high-lift aircraft geometries has been presented. The HRLES method was evaluated for both the free air and wind tunnel configurations and its predictions were compared against experimental results from the QinetiQ tunnel and numerically against RANS and WMLES approaches. When used with appropriately refined grids, the HRLES method demonstrated very good agreement with the available experimental data, addressed some of the shortcomings in RANS approaches and was competitive with WMLES in terms of solution accuracy. In what follows, we detail the key findings and important conclusions to be drawn from the paper:

1) Examining the time-averaged aerodynamic forces and moments, in both the free air and the wind tunnel configurations, HRLES made modest improvements over RANS at the low angles-of-attack for pitching moment coefficient. Much more significant improvements are noted for HRLES at $C_{L,\max}$ and post-stall when compared with steady state RANS (SA) - RANS does not predict a pitch break at the post-$C_{L,\max}$ state in the free air configuration and a very large over-prediction is seen in the wind tunnel. Furthermore, HRLES is able to address the sharp loss of lift predicted by RANS at the two highest angles-of-attack which also corresponds to the sharp nose down pitching moment. Other than the low angles-of-attack, where WMLES tracks the experimental data better than HRLES in pitching moment coefficient, good agreement is shown across the board for HRLES and WMLES in the free air configuration. This holds true for the wind tunnel configuration as well, except for the higher angles-of-attack where WMLES shows improvement in the prediction of lift.

2) It is critical to refine the HRLES meshes in the outboard region of the wing specifically to address the outboard separation predicted by RANS and HRLES (on coarser grids) at the high angles-of-attack. The earlier transition from RANS to LES closure was able to prevent the flow from separating after refining the outboard region and removing the high aspect ratio slat wake mesh. The original (high-aspect ratio) slat wake mesh was found to be very detrimental to correctly capturing the flow over the outboard wing in particular - although not exclusively. The high aspect ratio forced the shielding function to enforce RANS mode for a prolonged extent downstream of the slat, thereby preventing 3D turbulent structure from developing in the slat wake which energizes the main wing boundary layer and prevent it from separating. Similarly, the choice of time-step size, of a low dissipation numerical scheme and of suitably low aspect ratio grids in regions where one intends to perform large eddy simulations - were all instrumental in achieving good agreement with the experimental data and WMLES. As a matter of fact, simply *"turning-on"* the HRLES model, effectively activating the shielding function, with the RANS grid and employing numerics more suited to RANS actually produced predictions that were far inferior to RANS. This often-used approach generated solutions at the high angles-of-attack with erroneous large-scale inboard and outboard separation. The importance of the inboard resolution was also noted at the post-stall

28

angle-of-attack in the free air case where the incipient corner flow separation only developed on the finest grid level studied.

3) Besides the spatial/temporal resolution requirements and low-dissipation numerics, additional sensitivities to the solution were noted. A focused study at $C_{L,\max}$ and post-stall showed different flow topologies were predicted with different underlying RANS SA closure models for HRLES. With the SA-RC-QCR2000 closure, the flow separates on the nacelle at $C_{L,\max}$ and post-stall while a different inboard flow topology is seen at post-stall. For the SA only closure, there was a sensitivity to how the simulation was initialized, namely, if initialized as a *"cold-start"* the flow remained attached for angles $> C_{L,\max}$ while if initialized from a steady-state RANS solution the flow separated on the nacelle for the same angles. A strong correlation between the strength of the nacelle chine vortex and whether inboard corner-flow separation was observed, highlighting the importance of the vortex on the separation mechanism. Additionally and possibly outside the scope of this paper but an interesting discovery nonetheless was that URANS with the closure SA-RC-QCR2000 on the HRLES grid did not separate outboard at the highest angle-of-attack in the free air configuration in contrast to all the steady state RANS with SA based closures that the were studied with the LAVA solver.

4) Excellent qualitative agreement was obtained when comparing the streamlines from the HRLES CFD and the oil-flow photographs from the QinetiQ experiment at $C_{L,\max}$ and post-stall. Despite the noted differences in the tunnel environments, many of the salient flow topology characteristics were captured by the HRLES, in stark contrast to what was predicted by RANS simulations. At the highest angle-of-attack, the vortices produced by the fully-formed flow separation on the fuselage and inboard region of the wing are well-represented by HRLES.

This paper has demonstrated the suitability of HRLES for high-lift aircraft geometry applications when used with appropriately refined grids, time steps, and low-dissipation numerics. The following items outlines some of the key findings and recommendations for moving towards HRLES best practices for future research efforts:

1) **Designing grids suitable for HRLES and meshing best practices**: The HRLES grid that was utilized for the current research effort on the CRM-HL was highly refined and modified compared to the original RANS grid. This paper has established that RANS meshing best practices are not suitable for a HRLES approach - at least for this test case and with the current LAVA framework. Adapting the RANS best practice was likely not optimal in terms of numerical robustness, grid quality and final mesh cell count. Future efforts should attempt to design purpose built HRLES grids with scale-resolving simulations in mind and low aspect ratio cells appropriate for LES outside the boundary layer, *i.e.* in an ideal world this would be a $y^+ = 1$ version of the WMLES grids with likely a coarser streamwise and spanwise grid spacing to keep the computational cost down and to be competitive with WMLES.

2) **Prudent choice of time-step size**: URANS and HRLES approaches that employ implicit time-stepping methods, like the BDF2 scheme utilized in this work, are not strictly bound by the acoustic CFL number in the choice of

29

time-step size in the way an explicit scheme would be. Therefore a compromise must be struck between using a time-step size large enough for the algorithm to be competitive with solvers using explicit schemes but conversely small enough to resolve the LES fluctuations and resolvable turbulent content. Using too large of a time-step resulted in excessive inboard separation at the post-stall state.

3) **Run out solutions for sufficiently long time interval:** This point applies not only to HRLES but all scale-resolving simulations. It is evident that particularly at the higher angles-of-attack in the wind tunnel configuration, approximately 50-70 CTU were required to obtain confidence in the stationarity of the first-order statistics of the solution.

4) **When is it cost effective to employ HRLES?**: An overview and analysis of the computational cost of RANS, HRLES and WMLES with the LAVA solver for the CRM-HL was provided in Ref. [13]. It was shown that HRLES run on best practice Grid H-D was 26× and 13× more expensive than a RANS steady state run on meshes Grid R-C and R-D, respectively. It is worth reiterating here that an ideal best practice HRLES mesh is likely to have a lower cell count than Grid H-D when considering the point raised in the first item above. It was shown that when comparing a URANS and HRLES run with the same time-step size, using same Grid H-D and same numerics, that HRLES gave superior predictions over URANS. Therefore, when considering a scale resolving time-step size, HRLES would be the preferred option especially considering that both methods would roughly be the same computational cost (there may be some differences in the stiffness of the Jacobian matrix used in the implicit scheme but this will be mesh and numerical scheme *etc* dependent). However, in practice URANS is utilized with a larger time-step size and therefore generally significantly cheaper than scale-resolving approaches such as HRLES. Finally, a strong case for HRLES can be made for the region of $C_{L,\max}$ and post-stall (nonlinear part of lift curve) based on the results presented in this paper. However, at the lower angles-of-attack (linear part of lift) curve, given the effectiveness of RANS - even with the above-mentioned improvements of HRLES in pitching moment coefficient - it may not as strongly warrant the increased computational cost of the scale resolving simulations. However, cost/accuracy for HRLES is objectively superior compared to RANS which instead of improving with grid resolution, showed, for the CRM-HL case, diminishing returns in terms of accuracy[37]. The HRLES is likely to improve the prediction of pitch moment coefficient at lower angles-of-attack as well - the flap separation reduces when a switch to LES closure is made, therefore a further targetted LES-friendly grid refinement is needed to evaluate this interesting aspect further.

5) **Large sensitivity persists due to the underlying RANS closure**: Although there was a limited number of other submissions to the HRLES HLPW4 TFG, there was quite a large spread in terms of the predicted results. The large sensitivity in underlying RANS closure and choice of shielding function needs to be investigated further to understand the mechanisms driving the differences to increase confidence in the predicted results. In terms of uncertainty in the RANS closure, this is a principle factor which needs to be resolved to improve

predictability for HRLES. This is consistent with the fact that as we see improvements as more of the simulated domain switching to LES - thereby reducing the dependence on the RANS closure and all its flaws that the hybrid approach *"inherits"*. As mentioned in the introduction, a previous HRLES study showed when moving to higher mesh resolutions, inferior predictions in the separated flow region were obtained[12]. This was not the case for the meshes considered in this work which shows the newer ZDES2020 Mode 2 EP shielding function has, to a certain extent, alleviated a previously known drawback of DDES methods. Finally, a hybrid RANS/LES approach with a significantly different closure model such as Menter Shear Stress Transport (SST) which was shown to provide improvements over SA could be in interesting avenue to pursue[37]. Many of the shortcomings of the SST closure in comparison to SA closure (such as larger stiffness for steady state solves) are insignificant when time-accurate simulations are performed.

In conclusion, this work constitutes a major step forward in meeting the goals of NASA's TTT-RCA goals of developing robust, accurate, and computationally feasible tools for predicting aerodynamics loads of high-lift configurations. An objective case has been made for HRLES as a viable approach for $C_{L,\mathrm{max}}$ and post-stall prediction of high-lift aircraft geometries.

Acknowledgments

References

[1] Clark, A. M., Slotnick, J. P., Taylor, N. J., and Rumsey, C. L., "Requirements and challenges for CFD validation within the High-Lift Common Research Model ecosystem," *AIAA Aviation 2020 Forum,* AIAA Paper 2020-2772, 2020. doi:10.2514/6.2020-2772.

[2] Rumsey, C. L., and Ying, S. X., "Prediction of high lift: review of present CFD capability," *Progress in Aerospace Sciences*, Vol. 38, No. 2, 2002, pp. 145–180. doi:10.1016/S0376-0421(02)00003-9.

[3] Rumsey, C. L., Slotnick, J. P., and Sclafani, A. J., "Overview and Summary of the Third AIAA High Lift Prediction Workshop," *Journal of Aircraft*, Vol. 56, No. 2, 2019, pp. 621–644. doi:10.2514/1.C034940.

[4] Slotnick, J., Khodadoust, A., Alonso, J., Darmofal, D., Gropp, W., Lurie, E., and Mavriplis, D., "CFD vision 2030 study: a path to revolutionary computational aerosciences," NASA CR–2014-218178, NASA, 2014.

[5] Slotnick, J. P., and Mavriplis, D., "A Grand Challenge for the Advancement of Numerical Prediction of High Lift Aerodynamics," *AIAA SciTech 2021 Forum,* AIAA Paper 2021-0955, 2021. doi:10.2514/6.2021-0955.

[6] Slotnick, J., and Heller, G., "Emerging opportunities for predictive CFD for off-design commercial airplane flight characteristics," *Proceedings of the 54th 3AF International Conference on Applied Aerodynamics*, 2019, pp. 25–27.

[7] Rumsey, C., Slotnick, J., and Woeber, C., "HLPW-4/GMGW-3: Overview and Workshop Summary," *AIAA Aviation 2022 Forum,* AIAA Paper 2022-3295, 2022. doi:10.2514/6.2022-3295.

[8] Mauery, T., Alonso, J., Cary, A., Lee, V., Malecki, R., Mavriplis, D., Medic, G., Schaefer, J., and Slotnick, J., "A Guide for Aircraft Certification by Analysis," NASA CR-20210015404, NASA, 2021.

[9] Rumsey, C., "4th AIAA High Lift Prediciton Workshop," , 2021. URL `https://hiliftpw.larc.nasa.gov/`.

[10] Konig, B., Fares, E., Murayama, M., Ito, Y., Yokokawa, Y., Yamamoto, K., and Ishikawa, K., "Lattice-Boltzmann simulations of the JAXA JSM high-lift configuration," *34th AIAA Applied Aerodynamics Conference,* AIAA Paper 2016-3721, 2016. doi:10.2514/6.2016-3721.

[11] Cary, A. W., Yousuf, M., Li, P., and Mani, M., "Current practice unstructured grid CFD results for 3rd AIAA High Lift Prediction Workshop," *2018 AIAA Aerospace Sciences Meeting,* AIAA Paper 2018-1037, 2018. doi:10.2514/6.2018-1037.

[12] Ghate, A. S., Housman, J. A., Stich, G.-D., Kenway, G., and Kiris, C. C., "Scale resolving simulations of the NASA Juncture Flow Model using the LAVA solver," *AIAA Aviation 2020 Forum,* AIAA Paper 2020-2735, 2020. doi:10.2514/6.2020-2735.

[13] Kiris, C. C., Ghate, A. S., Duensing, J. C., Browne, O. M., Housman, J. A., Stich, G.-D., Kenway, G., Dos Santos Fernandes, L. M., and Machado, L. M., "High-Lift Common Research Model: RANS, HRLES, and WMLES perspectives for CLmax prediction using LAVA," *AIAA SciTech 2022 Forum,* AIAA Paper 2022-1554, 2022. doi:10.2514/6.2022-1554.

[14] Ollivier-Gooch, C., and Coder, J., "Fixed-Grid RANS TFG," , 2022. URL `https://hiliftpw.larc.nasa.gov/Workshop4/WorkshopPresentations/03_GMGW3_HLPW4_RANS.pdf`, accessed: 2022-05-08.

[15] Jensen, J. C., Stich, G.-D., Housman, J. A., Denison, M., and Kiris, C. C., "LAVA Simulations for the 3rd AIAA CFD High Lift Prediction Workshop using Body Fitted Grids," *2018 AIAA Aerospace Sciences Meeting,* AIAA Paper 2018-2056, 2018. doi:10.2514/6.2018-2056.

[16] Lacy, D. S., and Clark, A. M., "Definition of Initial Landing and Takeoff Reference Configurations for the High Lift Common Research Model (CRM-HL)," *AIAA Aviation 2020 Forum,* AIAA Paper 2020-2771, 2020. doi:10.2514/6.2020-2771.

[17] Evans, A., Lacy, D., Smith, I., and Rivers, M., "Test Summary of the NASA Semi-Span High-Lift Common Research Model at the QinetiQ 5-Metre Low-Speed Wind Tunnel," *AIAA Aviation 2020 Forum,* AIAA Paper 2020-2770, 2020. doi:10.2514/6.2020-2770.

[18] Kiris, C. C., Housman, J. A., Barad, M. F., Brehm, C., Sozer, E., and Moini-Yekta, S., "Computational framework for launch, ascent, and vehicle aerodynamics (LAVA)," *Aerospace Science and Technology*, Vol. 55, 2016, pp. 189–219. doi:10.1016/j.ast.2016.05.008.

[19] Browne, O. M. F., Housman, J. A., Kenway, G. K. W., Ghate, A. S., and Kiris, C. C., "A Hybrid RANS-LES Perspective for the High Lift Common Research Model Using LAVA," *AIAA Aviation 2022 Forum,* AIAA Paper 2022-3523, 2022. doi:10.2514/6.2022-3523.

[20] Deck, S., and Renard, N., "Towards an enhanced protection of attached boundary layers in hybrid RANS/LES methods," *Journal of Computational Physics*, Vol. 400, 2020, p. 108970. doi:10.1016/j.jcp.2019.108970.

[21] Spalart, P. R., Deck, S., Shur, M. L., Squires, K. D., Strelets, M. K., and Travin, A., "A new version of detached-eddy simulation, resistant to ambiguous grid densities," *Theoretical and Computational Fluid Dynamics*, Vol. 20, No. 3, 2006, p. 181. doi:10.1007/s00162-006-0015-0.

[22] Deck, S., "Recent improvements in the zonal detached eddy simulation (ZDES) formulation," *Theoretical and Computational Fluid Dynamics*, Vol. 26, No. 6, 2012, pp. 523–550. doi:10.1007/s00162-011-0240-z.

[23] Ghate, A. S., Kenway, G. K., Stich, G.-D., Browne, O. M., Housman, J. A., and Kiris, C. C., "Transonic lift and drag predictions using Wall-Modelled Large Eddy Simulations," *AIAA SciTech 2021 Forum,* AIAA Paper 2021-1439, 2021. doi:10.2514/6.2021-1439.

[24] Housman, J. A., Stich, G.-D., Kocheemoolayil, J. G., and Kiris, C. C., "Predictions of Slat Noise from the 30P30N at High Angles of Attack using Zonal Hybrid RANS-LES," *25th AIAA/CEAS Aeroacoustics Conference,* AIAA Paper 2019-2438, 2019. doi:10.2514/6.2019-2438.

[25] Stich, D., Housman, J. A., Kocheemoolayil, J. G., Barad, M. F., Cadieux, F., and Kiris, C. C., "Application of Lattice Boltzmann and Navier-Stokes Methods to NASA's Wall Mounted Hump," *2018 Fluid Dynamics Conference,* AIAA Paper 2018-3855, 2018. doi:10.2514/6.2018-3855.

[26] Spalart, P., and Allmaras, S., "A one-equation turbulence model for aerodynamic flows," *30th Aerospace Sciences Meeting and Exhibit,* AIAA Paper 1992-439, 1992. doi:10.2514/6.1992-439.

[27] Allmaras, S. R., and Johnson, F. T., "Modifications and clarifications for the implementation of the Spalart-Allmaras turbulence model," *Seventh International Conference on Computational Fluid Dynamics (ICCFD7)*, Vol. 1902, Big Island, HI, 2012.

[28] Shur, M. L., Strelets, M. K., Travin, A. K., and Spalart, P. R., "Turbulence modeling in rotating and curved channels: assessing the Spalart-Shur correction," *AIAA Journal*, Vol. 38, No. 5, 2000, pp. 784–792. doi:10.2514/2.1058.

[29] Spalart, P. R., "Strategies for turbulence modelling and simulations," *International Journal of Heat and Fluid Flow*, Vol. 21, No. 3, 2000, pp. 252–263. doi:10.1016/S0142-727X(00)00007-2.

[30] Spalart, P. R., and Garbaruk, A. V., "Correction to the Spalart–Allmaras Turbulence Model, Providing More Accurate Skin Friction," *AIAA Journal*, Vol. 58, No. 5, 2020, pp. 1903–1905. doi:10.2514/1.J059489.

[31] Ghate, A., Housman, J., Stich, G.-D., Kenway, G., and Kiris, C., "Scale Resolving Simulations of Corner-Flow Separation in a Wing-Body Juncture," , 2020. URL `https://www.nas.nasa.gov/pubs/ams/2020/09-10-20.html`, Advanced Modeling and Simulation Seminar Series.

[32] Stich, G.-D., Housman, J. A., Kocheemoolayil, J. G., Kiris, C. C., and Bridges, J. E., "Large-Eddy Simulation of Jet Surface Interaction Noise," *25th AIAA/CEAS Aeroacoustics Conference,* AIAA Paper 2019-2475, 2019. doi:10.2514/6.2019-2475.

[33] Housman, J. A., Stich, G.-D., and Kiris, C. C., "Jet noise prediction using hybrid RANS/LES with structured overset grids," *23rd AIAA/CEAS Aeroacoustics Conference,* AIAA Paper 2017-3213, 2017. doi:10.2514/6.2017-3213.

[34] Brehm, C., Barad, M. F., Housman, J. A., and Kiris, C. C., "A comparison of higher-order finite-difference shock capturing schemes," *Computers & Fluids*, Vol. 122, 2015, pp. 184–208. doi:10.1016/j.compfluid.2015.08.023.

[35] Shu, C.-W., "High order weighted essentially nonoscillatory schemes for convection dominated problems," *SIAM review*, Vol. 51, No. 1, 2009, pp. 82–126. doi:10.1137/070679065.

[36] Deng, X., and Zhang, H., "Developing high-order weighted compact nonlinear schemes," *Journal of Computational Physics*, Vol. 165, No. 1, 2000, pp. 22–44. doi:10.1006/jcph.2000.6594.

[37] Duensing, J. C., Housman, J. A., Dos Santos Fernandes, L. M., Machado, L. M., and Kiris, C., "A Reynolds-Averaged Navier-Stokes Perspective for the High Lift-Common Research Model Using the LAVA Framework," *AIAA Aviation 2022 Forum,* AIAA Paper 2022-3742, 2022. doi:10.2514/6.2022-3742.

[38] Jiang, G.-S., and Shu, C.-W., "Efficient implementation of weighted ENO schemes," *Journal of Computational Physics*, Vol. 126, No. 1, 1996, pp. 202–228. doi:10.1006/jcph.1996.0130.

[39] Ghate, A. S., Kenway, G. K. W., Stich, G.-D., Maldonado, D., and Kiris, C. C., "A Wall-Modeled LES Perspective for the High Lift Common Research Model Using LAVA," *AIAA Aviation 2022 Forum,* AIAA Paper 2022-3434, 2022. doi:10.2514/6.2022-3434.

[40] Koklu, M., Lin, J. C., Hannon, J. A., Melton, L. P., Andino, M. Y., Paschal, K. B., and Vatsa, V. N., "Investigation of the Nacelle/Pylon Vortex System on the High-Lift Common Research Model," *AIAA Journal*, Vol. 59, No. 9, 2021, pp. 3748–3763. doi:10.2514/1.J059869.

[41] Maldonado, D., Viken, S. A., Housman, J. A., Hunter, C. A., Duensing, J. C., Frink, N. T., Jensen, J. C., McMillin, S. N., and Kiris, C. C., "Computational Simulations of a Mach 0.745\Transonic Truss-Braced Wing Design," *AIAA SciTech 2020 Forum,* AIAA Paper 2020-1649, 2020. doi:10.2514/6.2020-1649.

[42] Maldonado, D., Hunter, C., Housman, J. A., Viken, S. A., Piotrowski, M. G., McMillin, S. N., Kiris, C. C., and Milholen, W. E., "Improvements in Simulating a Mach 0.80 Transonic Truss-Braced Wing Configuration using the Spalart-Allmaras and k-ω SST Turbulence Models," *AIAA SciTech 2021 Forum,* AIAA Paper 2021-1531, 2021. doi:10.2514/6.2021-1531.

[43] Housman, J. A., and Kiris, C. C., "Slat Noise Predictions using Higher-Order Finite-Difference Methods on Overset Grids," *22nd AIAA/CEAS Aeroacoustics Conference,* AIAA Paper 2016-2963, 2016. doi:10.2514/6.2016-2963.

[44] Koch, J. R., Dumlupinar, E., Housman, J. A., Kiris, C. C., Patel, M. M., Kleb, B., Brauckmann, G. J., and Alter, S. J., "CFD analysis of Space Launch System solid rocket booster separation within the Langley Unitary Plan Wind Tunnel," *AIAA Aviation 2021 Forum,* AIAA Paper 2021-2966, 2021. doi:10.2514/6.2021-2966.

[45] Housman, J. A., and Kiris, C. C., "Numerical Simulations of Shock/Plume Interaction Using Structured Overset Grids," *33rd AIAA Applied Aerodynamics Conference,* AIAA Paper 2015-2262, 2015. doi:10.2514/6.2015-2262.